A&A 528, A3 (2011)
DOI: 10.1051/0004-6361/201015897

Astronomy & Astrophysics

VLT integral field spectroscopy of embedded protostars: using near-infrared emission lines as tracers of accretion and outflow⋆,⋆⋆

C. J. Davis[1], B. Cervantes[1,2], B. Nisini[3], T. Giannini[3], M. Takami[4], E. Whelan[5], M. D. Smith[6], T. P. Ray[7], A. Chrysostomou[1], and T. S. Pyo[8]

[1] Joint Astronomy Centre, 660 North A'ohōkū Place, University Park, 96720 Hilo, Hawaii, USA
e-mail: c.davis@jach.hawaii.edu
[2] Department of Physics and Astronomy, University of Victoria, Victoria BC, Canada
[3] INAF-Osservatorio Astronomico di Roma via di Frascati 33, 00040, Monteporzio Catone, Italy
[4] Institute of Astronomy and Astrophysics, Academia Sinica, PO Box 23-141, 10617 Taipei, Taiwan
[5] Laboratoire d'Astrophysique de Grenoble, UMR 5571, BP 53, 38041 Grenoble Cedex 09, France
[6] Centre for Astrophysics & Planetary Science, School of Physical Sciences, University of Kent, Canterbury CT2 7NR, UK
[7] Dublin Institute for Advanced Studies, 31 Fitzwilliam Place, Dublin 2, Ireland
[8] Subaru Telescope, National Astronomical Observatory of Japan, 650 North A'ohōkū Place, HI 96720, Hilo, USA

Received 8 October 2010 / Accepted 24 December 2010

ABSTRACT

Aims. We present near-infrared spectroscopy of the forbidden emission line (FEL) and molecular hydrogen emission line (MHEL) regions at the bases of Herbig-Haro (HH) jets from seven embedded protostars: SVS 13 (the HH 7-11 progenitor), HH 26-IRS, HH 34-IRS, HH 72-IRS, HH 83-IRS, HH 300-IRS (IRAS 04239+2436) and HH 999-IRS (IRAS 06047-1117)
Methods. The integral field spectrograph, SINFONI, on the European Southern Observatory's Very Large Telescope (VLT) was used to characterise jet parameters in these formative regions, where the jets are collimated and accelerated.
Results. We find considerable differences in the spectra of HH 83-IRS when compared to the other six sources; CO bandhead and atomic permitted lines from Ca I, Na I, Mg I and Al I are observed in emission in all but HH 83-IRS, where they are detected in absorption. It is likely that this source is more evolved than the others (or at the very least considerably less active). Strong CO bandhead emission is also detected in emission in the other six sources, while extended H_2 ro-vibrational and [Fe II] forbidden emission lines trace the outflows (only the HH jet from HH 83-IRS is undetected). CO bandhead and Brγ emission peaks are in most cases coincident with the jet source continuum position, consistent with excitation in an accretion disk or accretion flow. However, in the closest source, HH 300-IRS, we do find evidence for excitation in the outflow: here the emission peak is offset by 3.6(±0.7) AU along the flow axis. We also note a correlation between CO and Mg I, Na I and Ca I intensities, which supports the idea that these atomic permitted lines are associated with accretion disks. From H_2 and [Fe II] images we measure jet widths and derive upper limits to flow component opening angles. Although we do not find that the ionised [Fe II] component is consistently narrower than the H_2 flow component, we do find that narrower H_2 and/or [Fe II] flow components are associated with higher radial velocities (as reported in the literature). Flow opening angles, over the first few hundred AU in each source, are measured to be in the range 21°–42° in both H_2 and [Fe II]. Finally, from our 3-D data we are also able to map the extinction and electron density at the base of the outflows from some of our targets: within a few hundred AU, both decrease sharply with distance from the source.
Conclusions. It seems clear that collimated atomic *and* molecular jets, which may initially exhibit a wide opening angle, are a feature of outflows from Class I protostars, Class II T Tauri stars, and possibly even Class 0 sources, and that these jets can be traced to within a few hundred AU of the driving source. A common jet collimation and acceleration mechanism seems inescapable for all stages of low mass star formation.

Key words. shock waves – stars: formation – stars: protostars – Herbig-Haro objects – ISM: jets and outflows – stars: mass-loss

1. Introduction

When a star forms, centrifugal and magnetic forces act together to launch Herbig-Haro (HH)-type jets along magnetic field lines from a region very close to the accreting source. The jets extract mass and angular momentum from the underlying disk, thereby facilitating disk accretion; some fraction of the jet may also be ejected from the star itself, thereby removing angular momentum from the central object and producing the slow spin speeds observed in classical T Tauri stars (Matt & Pudritz 2008a, b).

To better understand this accretion/ejection dynamic, and ultimately to constrain and distinguish between models of disk-winds, where the jet is launched from a large spread of disk radii ($R \sim 0.1$–10 AU, Pudritz & Norman 1986; Garcia et al. 2001; Safier 1993; Ferreira 1997) and X-winds, where the ejection occurs from a single annulus at the inner edge of the disk ($R < 0.1$ AU, Shu et al. 1991; Shang et al. 2002), spectroscopic techniques have been employed to probe the kinematics and

⋆ Data obtained at the VLT under project 078.C-0390(B)
⋆⋆ Appendices are only available in electronic form at http://www.aanda.org

Table 1. Log of the SINFONI observations, plus target information.

Source	MHO[a]	RA (J2000)	Dec (J2000)	d^a (pc)	UT Date of Observations	Integ[b] (sec)	PA[c] (degs)	AM[d]	Standard[e] (Hip)	Seeing[e]	Ref.
HH 34-IRS	103	5:35:29.88	–06:26:57.8	450	18, 22 Oct. 2006	2400	77	1.3	026213	0.42″	3, 4
HH 300-IRS	732	4:26:56.30	24:43:35.2	140	22 Oct. 2006	1200	–31	1.5	043763	0.66″	3
SVS 13	512	3:29:03.75	31:16:04.0	220	6 Oct. 2006	2400	69	1.8	041620	0.63″	1, 2
HH 72-IRS	1407	7:20:08.35	–24:02:22.9	1500	20 Oct. 2006	1200	4	1.1	033641	0.29″	5
HH 999-IRS	1329/30	6:07:08.51	–11:17:50.9	500	22 Oct. 2006	1200	60	1.2	032112	0.37″	6
HH 26-IRS	326	5:46:03.63	–00:14:49.3	400	22 Oct. 2006	1200	–48	1.1	026579	0.64″	5
HH 83-IRS	181	5:33:32.58	–06:29:45.4	450	24 Oct. 2006	1200	38	1.1	031028	0.41″	3

Notes. [(a)] MHO catalogue reference (Davis et al. 2010), and the distance to the target adopted in this paper. [(b)] Total integration time spent on source. [(c)] Position Angle of the IFS, measured East of North. [(d)] Mean airmass during the observations on the source. [(e)] Standard star used to calibrate the source data, and the seeing measured from the standard at 2.12 μm.

References. 1. Bally et al. (1996); 2. Noriega-Crespo et al. (2002); 3. Reipurth et al. (2000); 4. Reipurth et al. (2002); 5. Davis et al. (1997); 6. Yun et al. (2001).

excitation at the bases of jets, from Class II T Tauri stars (Hirth et al. 1997; Takami et al. 2001, 2004; Pyo et al. 2003, 2006; Woitas et al. 2002; Whelan et al. 2004; Beck et al. 2008; Agra-Amboage et al. 2009) but also recently from their more embedded Class I counterparts, the protostars (Davis et al. 2001, 2003, 2006; Pyo et al. 2005, 2009; Takami et al. 2006; Podio et al. 2006; Antoniucci et al. 2008; Garcia Lopez et al. 2008). [Fe II] forbidden and H_2 ro-vibrational emission lines are found to be bright at the base of each jet, although the two species clearly trace very different flow components. The [Fe II] derives from a forbidden emission-line (FEL) region associated with hot, dense, partially-ionised, high-velocity gas ($T \sim 10\,000$ K; electron densities $\sim 10^5$ cm^{-3}; radial velocities approaching 100–200 km s^{-1}), while the H_2 traces the molecular hydrogen emission-line (MHEL) region associated with low-excitation, shocked (or possibly fluoresced) molecular gas at much lower velocities ($T \sim 2\,000$ K; densities $\geq 10^3$ cm^{-3}; $v_{\rm rad}$ ~10–50 km s^{-1}).

In both X-wind and disk-wind models the wind initially expands, is magnetically accelerated and heated to $\sim 10^4$ K within a few AU of the source via ambipolar diffusion and/or by X-rays from the central star (X-winds: Shang et al. 2002; disk-winds: Safier 1993; Garcia et al. 2001). Re-collimation occurs at a point where the dynamical pressure balances the magnetic pressure, i.e. close to the Alfvén radius, which is probably within a few astronomical units (AU) of the source (note that the Alfvén radius is a few times the launching radius, which has to be deep enough within the gravitational potential to produce the observed high jet speeds). At this point a radiative "collimation shock" may form (Ouyed & Pudritz 1994). Further downwind, where internal shocks heat and ionise the gas, line emission dominates the cooling and HH and/or H_2 jets are often observed.

X-wind and disk-wind models usually attempt to explain characteristics derived from high-resolution studies of jets from Class II young stellar objects (YSOs) (see for example the review of Cabrit 2009). They have yet to be applied to emission-line regions at the bases of jets from Class I protostars. This is largely due to a lack of observational data; note that at visible wavelengths Class I sources are usually hidden behind tens of magnitudes of extinction. To address this paucity of data, we have therefore surveyed a handful of protostars in the H and K-bands with the SINFONI integral field spectrograph (IFS). With seeing limited observations one can not expect to probe the spatial (few AU) scales needed to clearly discriminate between X-wind and disk-wind scenarios. However, one is able to investigate the inner propagation region, where the jet has not yet had time to strongly interact with the ambient medium and thus retains information on its acceleration mechanism. The widths of atomic and molecular jet components, their opening angles, the electron density and the mass flux are potentially also measurable quantities. Spatial information may also be acquired by using spectro-astrometric techniques (e.g. Hirth et al. 1997; Davis et al. 2001; Whelan et al. 2004).

In this paper we present new, deep, 2-dimensional H and K-band spectroscopy of seven outflow sources. In Sect. 2 we describe the observations and target sample, in Sect. 3 we examine images and spectra extracted from our data cubes, measuring flow component opening angles, mass-loss rates, the extinction and the electron density at the base of each jet, in Sect. 4 we discuss the data in terms of jet models and episodic accretion and outflow.

2. Observations

2.1. Integral field spectroscopy with SINFONI

Data were obtained using the IFS SINFONI at the ESO Very Large Telescope (UT-4) at Paranal, Chile in October 2006 (see Table 1 for details). The seeing was better than 0.7″ on each occasion, although some of the data were acquired through thin cirrus (variations in transparency less than 20%).

SINFONI houses a 2048×2048 pixel Hawaii 2RG array. The pixel scale measures 0.05″. An image slicer splits the input field into 32 slices; each slice is 64-pixels long and 2-pixels wide. The 64 × 64 pixel field of view in this mode is therefore ~3.2″ (note that in all extracted images the data have been re-sampled onto 0.05″ pixels). The image plane is rotatable, so with each target a position angle that aligns the jet axis along rows in the spatial plane was used (Table 1). All data were acquired with a moderate-resolution $H + K$ band grating ($R \sim 1500$); this resolution spans a relatively broad wavelength range, 1.45–2.45 μm, though yields essentially no useful velocity information for our sources.

Observations were conducted in the standard object-sky-sky-object (ABB′A′) mode, the instrument being offset to blank sky in each case. This sequence was executed twice for all sources except HH 34-IRS and SVS 13, where it was observed four times. The exposure time for individual target and sky frames was 300 s except for our brightest target, SVS 13, where three

coadds of 100 s were used. Total on-source integration times are listed in Table 1.

The SINFONI data reduction pipeline was used to apply dark and bad pixel masks, to flat-field the data, to correct for optical distortions and to apply a wavelength calibration (using Xenon arc lamp images). The pipeline also subtracts sky frames from object frames and creates data cubes for each target and standard star. STARLINK[1] software was then used to correct for atmospheric absorption and to flux calibrate the data, using observations of B3V-B5V standard stars (Table 1). Briefly, source and standard star spectra were extracted from the data by collapsing the central portion of each cube. Hydrogen recombination lines (up to Br11) were removed from the standard star spectra before division by an appropriate normalised black-body and spectral alignment with the associated target spectra. The standard star spectra were then grown into 64 × 64 × 2048 pixel cubes and divided into the appropriate target cubes to correct for telluric absorption and to flux calibrate the data.

One of the benefits of IFS observing is that the images in each emission line – and in the continuum – are taken simultaneously; the seeing and transparency are therefore exactly the same, and of course all data are registered. Therefore, precise continuum subtraction is possible, and very clean images of the line emission peaks close to the source continuum can be acquired. If the seeing is fully sampled, then 2-D Gaussian fitting and/or cross-correlation techniques can also be used to measure the accurate positions of emission knots, so that the positions of H_2 and [Fe II] features relative to each other, but also relative to the source continuum, hydrogen recombination lines, CO ro-vibrational lines and the permitted emission lines of other atomic metals (Na I, Ca I, Mg I, etc.), can be established. (A positional accuracy of ~Seeing/$(2.35 \times SN)$ is possible, i.e. ~20 mas for good seeing [~0.5 arcsec] and a modest signal-to-noise ratio [$SN \sim 10$].)

2.2. Target selection

We have selected seven embedded sources (listed in Table 1) based on their association with HH objects and/or Molecular Hydrogen emission-line Objects (MHOs, see the recent on-line catalogue described in Davis et al. 2010[2]). From spectroscopic studies, SVS 13 (the HH 7-11 source), HH 300-IRS (IRAS 04239+2436), HH 34-IRS and HH 72-IRS are also known to be associated with MHEL and/or FEL regions (e.g. Davis et al. 2003; Takami et al. 2006; Antoniucci et al. 2008). A compact jet has been observed in Fabry-Perot images and spectroscopy of HH 26-IRS (Davis et al. 1997; Chrysostomou et al. 2008), while HH 999-IRS powers HH objects and a striking bipolar molecular outflow (HH 999-IRS is associated with IRAS 06047-1117; Yun et al. 2001). HH 83-IRS – possibly the most evolved source in our sample – drives a collimated jet associated with a bright, conical reflection nebula (Reipurth 1989; Reipurth et al. 2000). The HH knots associated with the jet from HH 83-IRS were found to have a lower density (and higher ionisation fraction) than those in the HH 34 jet, by an order of magnitude in both cases, as one might expect for a more evolved system (Podio et al. 2006) – although such characteritics could also be attributed to lower rates of accretion and ejection. Note that optical 3-D spectroscopy of HH 83 has also recently been presented by Movsessian et al. (2009). Source bolometric luminosities (discussed later in this paper) are consistent with low mass YSOs, with the exception of HH 72-IRS and possibly SVS 13, which are more likely to be intermediate-mass sources.

[1] http://starlink.jach.hawaii.edu/
[2] http://www.jach.hawaii.edu/UKIRT/MHCat/

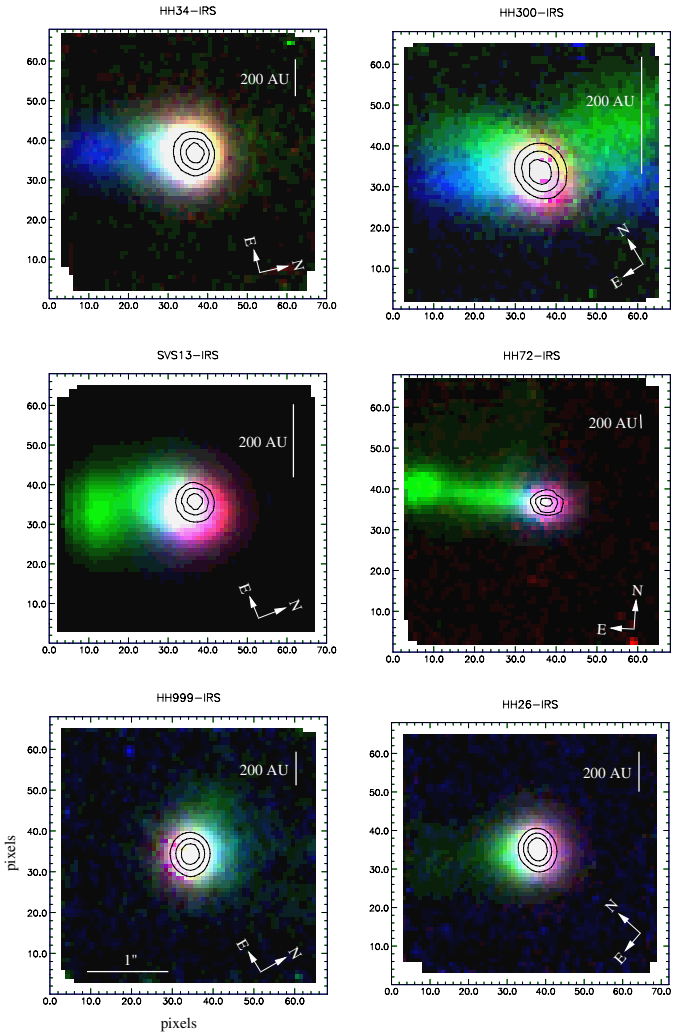

Fig. 1. Colour figures constructed from continuum-subtracted [Fe II] 1.644 μm (blue), H_2 2.122 μm (green) and Brγ 2.166 μm (red) images. The three images in each panel are scaled between the 10th and 95th percentile (consequently, regions where each line peaks tend to appear white). Contours of the continuum emission at 2.16 μm (i.e. adjacent to Brγ) are over-plotted at 50%, 75% and 90% the peak flux. Offsets are arbitrary and are in pixels. The horizontal axis in each panel is aligned with the nominal flow direction (listed in Table 1).

3. Results

3.1. Imaging of line emission at the base of each jet

The brightest emission lines associated with jets from young stars in the H and K-bands are produced by molecular hydrogen and singly-ionised iron (e.g. Caratti o Garatti et al. 2006; Takami et al. 2006; Antoniucci et al. 2008). Hydrogen recombination lines are also detected towards the central source. From each of the seven target IFS cubes we have therefore extracted images in the 1–0S(1) ro-vibrational line of H_2 at 2.122 μm, the 1.644 μm forbidden emission line of [Fe II], and Brγ at 2.166 μm. In each case a continuum image was extracted at wavelengths either side of the emission line; the average of these two continuum images was subtracted from the on-line image to produce continuum-subtracted images. These are presented in Fig. 1

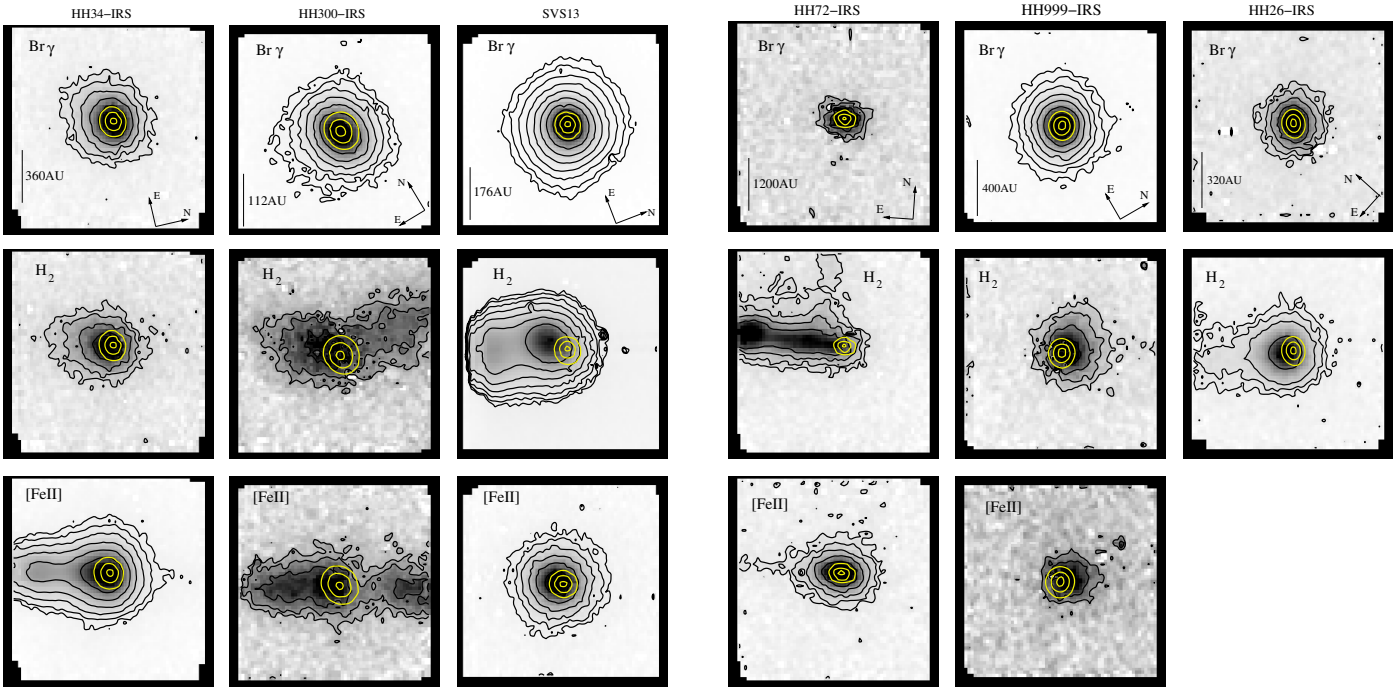

Fig. 2. Image plus contour plots showing (continuum-subtracted) Brγ 2.166 μm, H_2 2.122 μm and [Fe II] 1.644 μm emission towards HH 34-IRS, HH 300-IRS, SVS 13, HH 72-IRS and HH 999-IRS. Only Brγ 2.166 μm and H_2 2.122 μm images are shown for HH 26-IRS. For reference, contours showing the position of the continuum adjacent to each emission line are over-plotted in yellow. Black contours start at 3σ and increase in multiples of 2. The yellow continuum contours mark 50%, 75% and 95% of the peak flux in each continuum image. All figures are plotted to the same scale; the scale bar corresponds to 0.8″ in all data. The horizontal axis in each panel is aligned with the nominal flow direction.

as colour images, and in Fig. 2 as individual grey-scale images with contours plotted. Note, however, that [Fe II] emission was extremely weak toward HH 26-IRS (consistent with the spectroscopy of Antoniucci et al. 2008), and neither H_2 nor [Fe II] was observed in HH 83-IRS (so images for this source are not presented). Long-slit spectroscopy of HH 83-IRS were analysed by Podio et al. (2006), who likewise failed to detect line emission from the base of the jet. They note that the absence of [Fe II] emission may be due to a low jet density, since the Fe^+ levels have critical densities in excess of 10^4 cm^{-3}, or conversely to quenching of the emission if the density is too high. In HH 26-IRS, the lack of bright [Fe II] emission may also be consistent with the high H_2/Brγ ratio noted below, if the hydrogen recombination line is relatively weak because of modest gas excitation conditions at the jet base.

In Fig. 1 the contours mark the continuum position at 2.16 μm. In each panel in Fig. 2 the image and black contours show the distribution of line emission at the jet base; the position of the adjacent continuum is marked with yellow contours for reference. This nominal "source" position does, however, shift slightly with wavelength. In all cases, the continuum peak shifts along the flow axis (along the x-axis), moving downwind with decreasing wavelength. This shift is therefore largely due to extinction. Differential refraction – potentially a problem when observing at high airmass (for SVS 13 and HH 300-IRS) – was found to have an insignificant effect on the data (see Appendix A for details).

The colour images in Fig. 1 suggest that the distribution of H_2 and [Fe II] near each outflow source is complex and rather different from source to source: [Fe II] (the blue emission) appears to trace a collimated jet component in HH 34-IRS, with H_2 (green emission) enveloping the outer edges of the jet base – as one might expect if the H_2 is entrained along the walls of a collimated jet, or if it is excited in a disk-wind ejected at large disk radii. However, in HH 72-IRS (our most distant target), the reverse is seen, with faint [Fe II] evident around the base of a collimated H_2 jet. The jet is distinct in H_2 in HH 72-IRS, SVS 13 and (to a lesser extent) HH 26-IRS. Finally, in HH 300-IRS the axes of both lobes of this bipolar outflow appear to be traced in [Fe II] with H_2 emission detected only along the northern border of the jet lobes. If the H_2 represents entrained ambient gas, an inhomogeneous ambient medium may account for the lack of line emission along the southern walls of the jets. One should note, however, that Reipurth et al. (2000) identify HH 300-IRS as being a close binary, with a separation of 0.3″. In their high-resolution HST images HH 300 appears to be "wiggling" (they detect only the [Fe II] component of the jet); directional variability may therefore contribute to the off-axis emission detected here in H_2.

In Fig. 3 we plot profiles of the Brγ 2.166 μm, H_2 2.122 μm and [Fe II] 1.644 μm line emission along each jet axis; the continuum profile at 2.17 μm is also plotted for comparison. To produce these profiles, the continuum-subtracted images have been integrated vertically across the width of the flow. Multi-component Gaussian fits were then applied to each profile to measure peak positions and the extent of observed features (Tables 2 and 3).

In almost all sources we find that the Brγ emission peak is essentially coincident with the source continuum peak; the extent of the Brγ profile also matches than seen in the adjacent continuum profile. Both sets of profiles therefore represent an upper limit to the seeing. With a critical density in excess of 10^{10} cm^{-3}, Brγ traces very high excitation regions. However, whether these regions are associated with accretion "funnel" flows, the jet base, or a less collimated ionized wind, cannot be easily ascertain. We do record a slight offset between the Brγ and adjacent continuum peaks in our closest source, HH 300-IRS (note the offset of 0.026″ [3.6 AU] toward the north-eastern

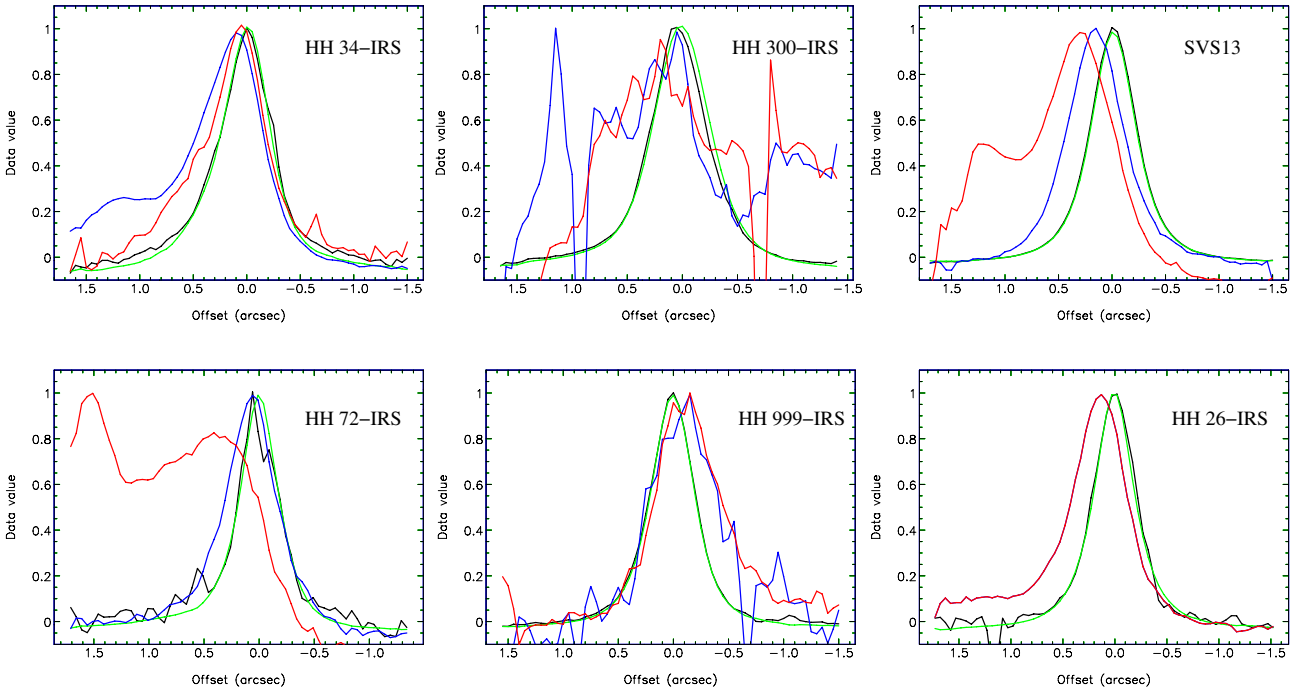

Fig. 3. Profiles of Brγ 2.166 μm (black), H_2 2.122 μm (red) and [Fe II] 1.644 μm (blue) line emission plotted along the jet axis for each source (the offset axis is measured in the plane of the sky). The profile of the continuum emission adjacent to Brγ is also plotted for reference (in green); this marks the nominal location of the embedded source, and gives an upper limit to the resolution along the flow axis. The profiles have been normalised to the peak flux. Offsets increase to the left in Figs. 1 and 2.

Table 2. Offsets of emission-line features along each jet axis, determined from multi-component Gaussian fits to the profiles shown in Fig. 3.

Source	α^a		Brγ^b	H_2 2.122 μm^b	[Fe II] 1.644 μm^b
HH 34-IRS	68°	Offset on sky	<0.008″	0.09″(±0.02″)	0.91″(±0.07″), 0.093″(±0.007″)
		Offset on sky	<3.6 AU	40.5(±9.0) AU	409(±31) AU, 41.8(±3.1) AU
		Offset along jet	<3.9 AU	43.7(±10) AU	441(±33) AU, 45.1(±3.3) AU
HH 300-IRS	60°	Offset on sky	0.026″(±0.005″)	<0.11″	0.22″(±0.04″), -1.1″(±0.1″)
		Offset on sky	3.6(±0.7) AU	<15 AU	30.8(±5.6) AU, -154(±14) AU
		Offset along jet	4.2(±0.8) AU	<17 AU	35.6(±6.5) AU, -178(±16) AU
SVS 13	40°	Offset on sky	<0.004″	1.16″(±0.03″), 0.32″(±0.02″)	0.168″(±0.005″)
		Offset on sky	<0.9 AU	225(±6.6) AU, 70.4(±4.4) AU	37.0(±1.1) AU
		Offset along jet	<1.4 AU	350(±10) AU, 109.5(±6.8) AU	57.6(±1.7) AU
HH 72-IRS	45°	Offset on sky	<0.008″	1.6″(±0.1″), 0.37″(±0.05″)	0.074″(±0.006″)
		Offset on sky	<12 AU	2400(±150) AU, 555(±75) AU	111(±9) AU
		Offset along jet	<17 AU	3394(±212) AU, 784(±106) AU	157(±13) AU
HH 999-IRS	45°	Offset on sky	<0.004″	–0.14″(±0.01″)	<0.02″
		Offset on sky	<2 AU	–70.7(±5.0) AU	<10 AU
		Offset along jet	<3 AU	–100(±7.0) AU	<14 AU
HH 26-IRS	65°	Offset on sky	<0.006″	0.15″(±0.01)″	...
		Offset on sky	<2.4 AU	60.0(±4.0) AU	...
		Offset along jet	<2.6 AU	66.2(±4.4) AU	...
HH 83-IRS	45°	Offset on sky	<0.007″	...	...
		Offset on sky	<3.1 AU	...	...
		Offset along jet			

Notes. [a] Orientation of the jet or outflow with respect to the line of sight (Reipurth 1989; Chrysostomou et al. 2000; Davis et al. 2003, and references therein). [b] Offsets of Brγ, H_2 and [Fe II] emission peaks relative to the interpolated continuum peak at 2.166 μm (the position of which is measured from the average of the continuum images extracted either side of the Brγ line). Negative values represent offsets to the right of the continuum in Figs. 1 and 2, positive to the left. The "offset on sky" values, given in arcseconds and in AU (using the adopted distances listed in Table 1), are uncorrected for flow orientation; the "offset along jet" values have been corrected for α.

Table 3. The extent along the flow axis of each Brγ, H_2 2.122 μm and [Fe II] 1.644 μm emission peak listed in Table 2.

Source	α^a		Brγ^a	H_2 2.122 μm^a	[Fe II] 1.644 μm^a
HH 34-IRS	68°	Extent on sky	0.60″(±0.01″)	0.75″(±0.03″)	1.3″(±0.15″), 0.60″(±0.02″)
		Extent on sky	270(±5) AU	337(±13) AU	585(±68) AU, 270(±9) AU
		Extent along jet	291(±5) AU	363(±14) AU	631(±73) AU, 291(±10) AU
HH 300-IRS	60°	Extent on sky	0.61″(±0.01″)	1.36″(±0.15″)	0.88″(±0.08″), 0.8″(±0.3″)
		Extent on sky	85(±2) AU	190(±21) AU	123 (±11) AU, 112(±42) AU
		Extent along jet	98(±2) AU	219(±24) AU	142 (±13) AU, 129(±48) AU
SVS 13	40°	Extent on sky	0.54″(±0.01″)	0.56″(±0.06″), 0.70″(±0.03″)	0.64″(±0.01″)
		Extent on sky	119(±2) AU	123(±13) AU, 154(±7) AU	141(±2) AU
		Extent along jet	185(±3) AU	191(±20) AU, 239(±11) AU	219(±3) AU
HH 72-IRS	45°	Extent on sky	0.49″(±0.02″)	1.2″(±0.4″), 0.80″(±0.08″)	0.57″(±0.02″)
		Extent on sky	735(±30) AU	1800(±600) AU, 1200(±120) AU	855(±30) AU
		Extent along jet	1040(±42) AU	2550(±850) AU, 1700(±170) AU	1210(±40) AU
HH 999-IRS	45°	Extent on sky	0.50″(±0.01″)	0.72″(±0.03″)	0.67″(±0.04″)
		Extent on sky	250(±5) AU	360(±15) AU	335(±20) AU
		Extent along jet	350(±7) AU	510(±20) AU	470(±30) AU
HH 26-IRS	65°	Extent on sky	0.50″(±0.02″)	0.65″(±0.02″)	...
		Extent on sky	200(±8) AU	260(±8) AU	...
		Extent along jet	221(±9) AU	287(±9) AU	...
HH 83-IRS	45°	Extent on sky	0.50″(±0.02″)	...	...
		Extent on sky	225(±9) AU	...	...
		Extent along jet			

Notes. $^{(a)}$ Orientation of the jet or outflow with respect to the line of sight. $^{(b)}$ Values are derived from the multi-component Gaussian fits to the profiles shown in Fig. 3. Note that these parameters are limited by the seeing (which has not been deconvolved from these data) and, in some cases (notably Brγ), the features may be unresolved. Values on sky, given in arcseconds and in AU (using the adopted distances listed in Table 1), are uncorrected for flow orientation; Values along the jet axis have been corrected for the flow inclination angle, α.

flow lobe). In this object the line emission may derive from the outflow. Similar offsets could also be present in some of the other, more distant sources; we may simply lack the resolution to observe these. Note also that recent VLTI observations of Herbig Ae/Be stars suggest that Brγ is more likely to be associated with a wind than with an accretion flow (Tatulli et al. 2007; Kraus et al. 2008; Benisty et al. 2010). Spatially extended Brγ has also very recently been observed in some low-mass T Tauri stars (Beck et al. 2010).

In Fig. 3 the H_2 and [Fe II] profiles are clearly extended along the flow axis (see Tables 2 and 3 for details); profile peaks are shifted downwind and therefore these emission lines must trace the outflow. In some cases the innermost H_2 feature is further from the source than the innermost [Fe II] peak (SVS 13, HH 72-IRS and possibly HH 999-IRS), although in HH 34-IRS the H_2 and [Fe II] emission peaks are almost coincident. The HH 34 jet is thought to be orientated close to the plane of the sky (Eislöffel & Mundt 1992), so flow inclination is unlikely to be the cause of this.

The offsets in Table 2 are generally consistent with those reported in previous spectro-astrometric studies (e.g. Davis et al. 2001, 2003; Takami et al. 2006), even though the new values may include off-axis emission in the collapsed IFS profiles not covered by the narrow slits used in the earlier studies. In their AO-corrected NACO long-slit spectroscopy of the SVS 13 jet, Davis et al. (2006) measure offsets of 0.29″(±0.01″) and 0.061″(±0.004″) for the first H_2 and [Fe II] peaks along the jet axis (note that these offsets are with respect to the adjacent continuum emission, and are not corrected for flow inclination angle). We simulate their 0.172″-wide slit by extracting profiles averaged across just the central four rows in the SINFONI data. In these new profiles, the inner-most H_2 and [Fe II] peaks are offset by 0.29″(±0.04 ″) and 0.10″(±0.02″) from the adjacent continuum peaks. Within the errors (the H_2 profile in particular comprises multiple components and cannot be fit with a single Gaussian), these offsets are consistent with the relatively low proper motions measured by Davis et al.: 0.03″/year (31 km s^{-1} at a distance of 220 pc) for the H_2 feature, and <0.02″/year (<20 km s^{-1}) for the [Fe II] feature. Note that the SINFONI and NACO observations were separated by just 1.72 years.

3.2. The widths and opening angles of each jet component

From the continuum-subtracted SINFONI images we have also measured the width of each jet component, by extracting 2-pixel (0.1″)-wide vertical slices and fitting a single Gaussian to each slice profile. The widths (which correspond to the full width, or full opening angle, of the flow) are plotted against de-projected distance from the source continuum position (i.e. corrected for flow inclination angle) in Fig. 4. These jet widths are deconvolved from the effects of seeing, using a seeing estimate measured from extracted continuum images in the *H*- and *K*-bands. The jet width therefore approaches zero in some of the plots.

In two of the six sources (HH 34-IRS and HH 26-IRS) the width of the H_2 flow component increases sharply with distance; by comparison, the [Fe II] jet width remains constant for HH 34-IRS and was too weak in HH 26-IR for detailed analysis. The reverse is seen in two other sources (HH 72-IRS and SVS 13), where only the [Fe II] flow component broadens with distance.

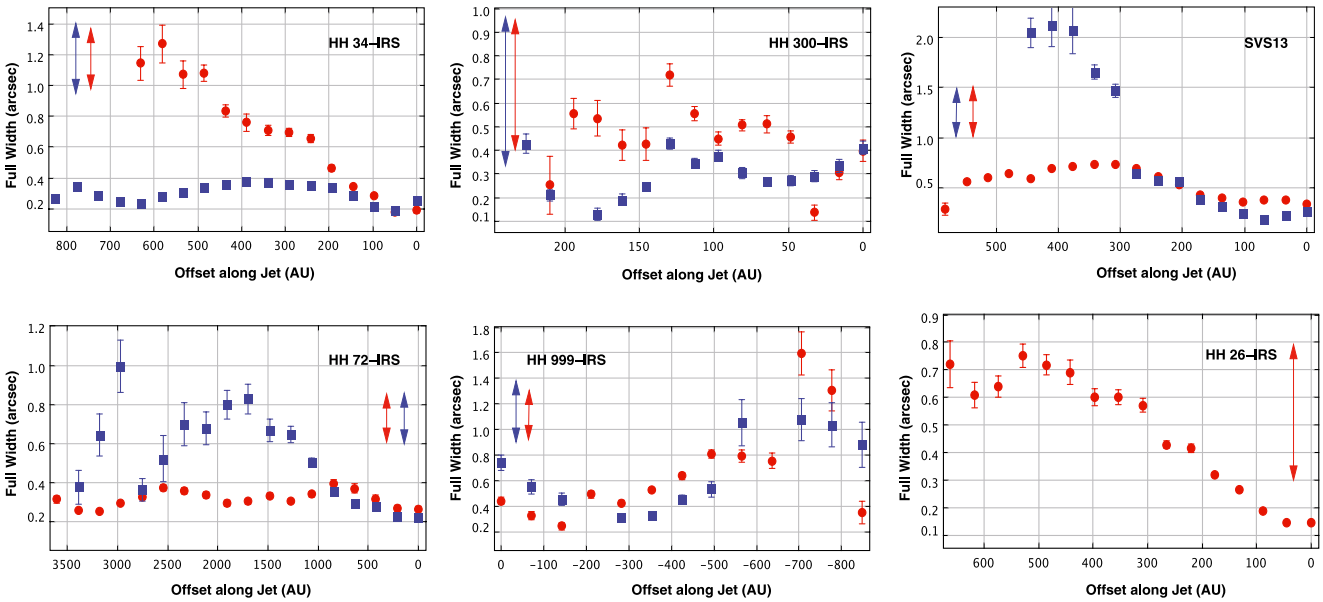

Fig. 4. Widths of the H_2 2.122 μm and [Fe II] 1.644 μm jet components plotted against distance from each source, corrected for flow inclination angle and seeing. Filled red circles indicate H_2 data; blue squares show [Fe II] data. The arrows show the effective angular resolution (FWHM) measured from Gaussian fits to continuum data in the *H* and *K*-bands. Zero offset in each *x*-axis corresponds to the source continuum position; positive offsets increase to the left in each panel in Figs. 1 and 2. Note that only the brighter, north-easterly flow lobe is plotted for HH 300-IRS.

Table 4. H_2 and [Fe II] jet widths and opening angles.

1 Source	2 L_{bol}[a] ($L_\odot$)	3 Offset (AU)	4 W_{H2}[b] (arcsec)	5 θ_{H2}[c] (deg)	6 Range[d] (AU)	7 θ_{H2}(fit)[d] (deg)	8 Offset (AU)	9 $W_{[FeII]}$[b] (arcsec)	10 $\theta_{[FeII]}$[c] (deg)	11 Range[d] (AU)	12 $\theta_{[FeII]}$(fit)[d] (deg)
HH 34-IRS	12–45	48.5	0.17	<48	0-640	42(±4)	48.5	0.19	<84	...	...
HH 300-IRS	1.1–1.3	...	...	...	...	...	...	...	...	...	...
SVS13	50–80	103	0.35	<41	0-350	21(±4)	68.5	0.17	<30	0-280	22(±2)
HH 72-IRS	170–280	212	0.27	<87	...	...	212	0.22	<76	0-1700	25(±3)
HH 999-IRS	6.0	141	0.24	<46	0-780	37(±6)	282	0.30	<30	0-850	27(±3)
HH 26-IRS	4.6–9.2	44.1	0.14	<65	0-530	28(±2)	...	...	...	...	...
HH 83-IRS	10.5	...	...	...	...	...	..	...	...	...	...

Notes. [(a)] Source bolometric luminosity taken from the literature: see Reipurth (1989), Chrysostomou et al. (2000), Yun et al. (2001) and Antoniucci et al. (2008). [(b)] FWHM widths of the H_2 and [Fe II] flow components measured at the distances listed in Cols. 3 and 8, respectively. Values are corrected for seeing (see Fig. 4). [(c)] Upper limits on the flow component (full) opening angles, θ_{H2} and $\theta_{[FeII]}$, derived from the offsets and widths in Cols. 3, 4 (for H_2) and 8, 9 (for [Fe II]). [(d)] Flow component full opening angles derived from fits to the jet widths plotted in Fig. 4 (which have been corrected for seeing) over the range specified in Cols. 6 and 11.

In HH 999-IRS both flow components seem to broaden with distance, while in the remaining source, HH 300-IRS, the H_2 and [Fe II] widths remain essentially constant. Therefore, on the spatial scales sampled by our observations (in the nearest source, HH 300-IRS, 1″ is equivalent to 140 AU; in the most distant source, HH 72-IRS, 1″ represents ∼1500 AU), we do find evidence for flow broadening – in at least one jet component – in five of the six sources. However, we do not consistently find that the ionised jet component is narrower than the molecular flow component.

Of course, we may simply lack the spatial resolution needed to resolve these two flow components, particularly within the first ∼100 AU of the source where the H_2 and [Fe II] emission-line regions are most likely to be disparate; beyond 100 AU the flow may develop bow shocks and/or otherwise interact with the ambient medium in such a way as to mix the two emission-line regions.

In some targets we do find that the narrower flow components are accompanied by emission at high velocities (as reported in the literature). For example, in echelle spectroscopy of HH 72-IRS the [Fe II] line profile peaks at a radial velocity of ∼150 km s^{-1}; the H_2 profile is multi-peaked, with strong components observed at 60 km s^{-1} and 149 km s^{-1} (these velocities are uncorrected for flow inclination angle). Towards SVS 13, the [Fe II] profile peaks at a radial velocity of ∼141 km s^{-1}; the H_2 profile peaks at a much lower velocity (28 km s^{-1}), though the blue-shifted profile wing includes a weaker, secondary peak at ∼97 km s^{-1} (Davis et al. 2001, 2003).

In Table 4 we attempt to quantify the jet component full opening angles, θ_{H2} and θ_{FeII}, by firstly measuring the narrowest jet width along the flow axis. We use the (de-projected) distance associated with this width to calculate θ_{H2} and θ_{FeII}. Results are listed in Table 4. All values should, however, be viewed as upper limits because (a) we assume that the flow converges to zero

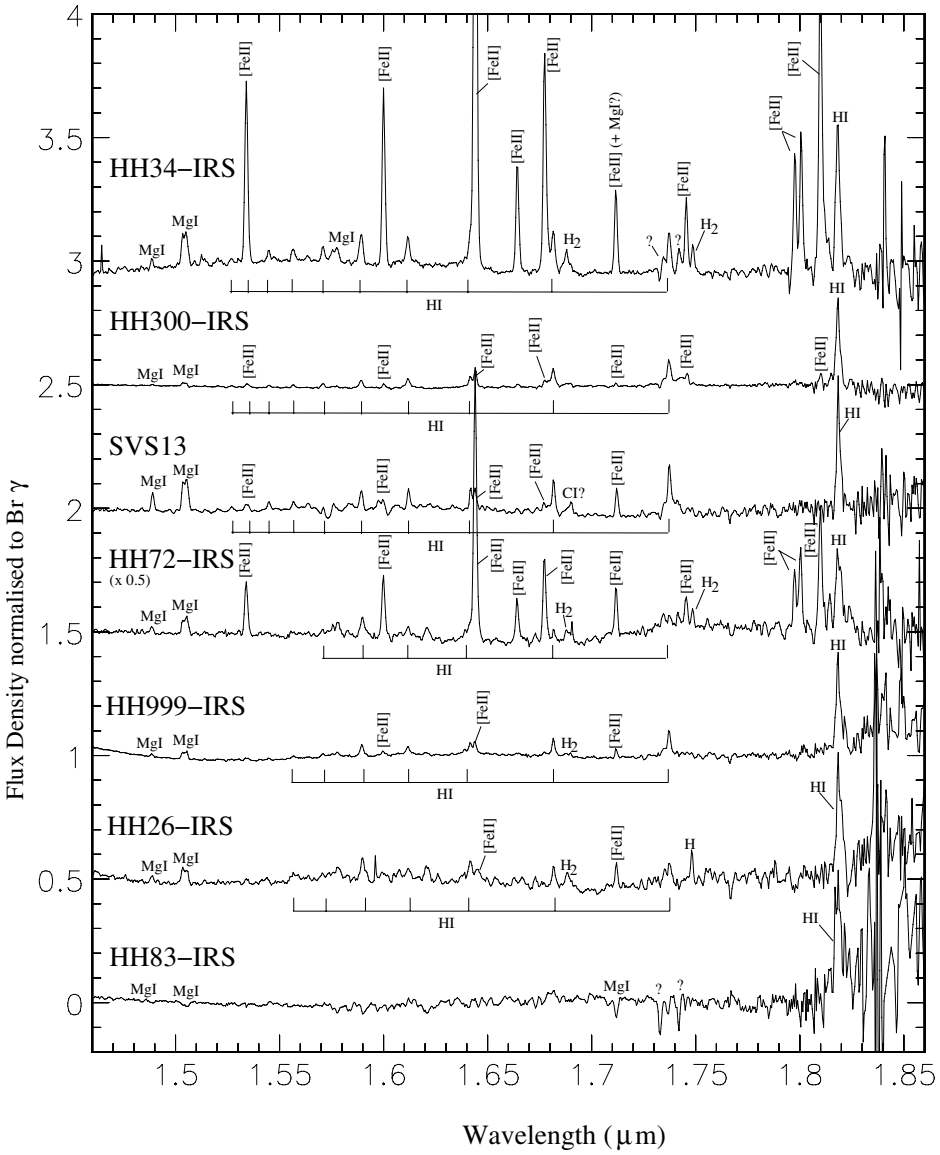

Fig. 5. *H*-band spectra extracted from each target over a 0.5″ square area centred on the continuum peak. The continuum emission has been fitted and removed and the spectra normalised to the peak flux density of Brγ. The spectrum of HH 72-IRS has been scaled by 0.5, and spectra have been separated vertically by a flux density of 0.5, to improve the overall clarity of the figure.

width at the source position, and (b) in many cases the jet width is close to being unresolved at its narrowest point.

More precise opening angles – albeit over greater jet lengths – can be measured by simply fitting a straight line to the data in Fig. 4. We exclude data points downwind where the flow appears to stop expanding (the extent of the flow over which the opening angles are calculated is listed in Table 4). θ_{H2}(fit) and θ_{FeII}(fit) represent mean values for the full opening angle of each flow component, measured over a few hundred AU along each jet axis. These values are certainly sensitive to the range of data points used; for HH 72-IRS, for example, θ_{FeII}(fit) is narrower if we exclude data beyond ~700 AU.

The values for θ_{H2}(fit) and θ_{FeII}(fit) listed in Table 4 are all in the range 21° to 42°; the flow components with no values listed in Cols. 7 and 12 in Table 4 presumably have narrower opening angles. Overall, the derived values are generally much smaller than the upper limits measured closer to the outflow source (θ_{H2} and θ_{FeII}). This result in not inconsistent with studies of jets from T Tauri stars, where HH jets exhibit larger opening angles when these are measured closer to the source, and smaller angles when measured further out (e.g. Ray et al. 1996; Dougados et al. 2000; Hartigan et al. 2004; Agra-Amboage et al. 2009).

Lastly, we note that there appears to be no clear correlation between source bolometric luminosity and flow opening angle (see Table 4), although obviously our data sample is limited.

3.3. Spectroscopy of the jet base and central engine

H- and *K*-band spectra towards each outflow source are displayed in Figs. 5–7; line intensities extracted from these spectra are presented in Appendix B, Tables B.1 and B.2. The spectra exhibit emission lines associated with both accretion and outflow. HH 83-IRS is clearly the most evolved source in our sample; it is associated with very little circumstellar matter, possessing instead photospheric absorption lines from Na I, Mg I, Ca I and

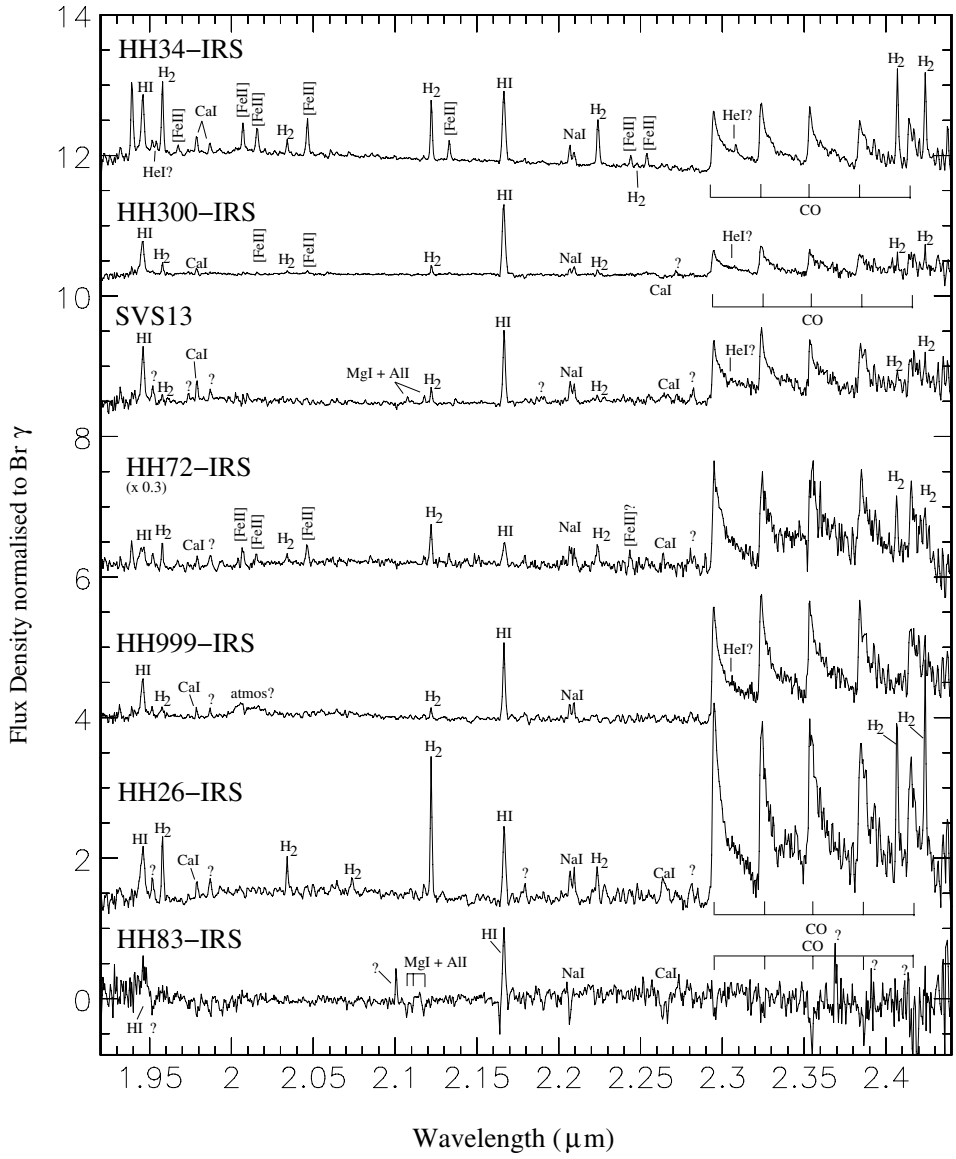

Fig. 6. *K*-band spectra extracted from each target over a 0.5″ square area centred on the continuum peak. The continuum emission has been fitted and removed and the spectra normalised to the peak flux density of Brγ. The spectrum of HH 72-IRS has been scaled by 0.3, and spectra have again been shifted vertically to improve the clarity of the figure.

Al I. It's spectrum is similar to that of a veiled late-type star (e.g. Doppmann et al. 2005).

In the remaining six sources only emission lines are detected. In addition to H I, like Antoniucci et al. (2008) we observed permitted atomic lines from Na I, Ca I, Mg I, Al I and possibly Ti I, the strongest of which are only 2–5 times weaker than Brγ (see Tables B.1 and B.2). These are probably circumstellar in origin, unlike the (veiled) photospheric absorption lines observed in HH 83-IRS. Because of their relatively low ionisation potentials, emission lines from Na I, Ca I and Mg I (5.1 eV, 6.1 eV and 7.6 eV, respectively) probably originate from larger disk radii than the hydrogen recombination lines (13.6 eV). Antoniucci et al. (2008) find that Na I lines are narrower than Brγ, as one would expect if the Brγ emission is associated with the inner, more ionised disk regions where Keplerian velocities are higher.

The first overtone ro-vibrational CO bandheads are seen in emission in all six of the embedded sources, and tentatively in absorption in HH 83-IRS. In protostars the CO lines are thought to be formed in the innermost regions of the disk or in a dense stellar wind (Carr 1989; Chandler et al. 1990; Najita et al. 1996), or in accretion flows between the inner disk surface and the central star (Martin 1997). The CO bands are also know to be highly variable in some young stars (e.g. Biscaya et al. 1997; Aspin et al. 2010).

H_2 ro-vibrational and [Fe II] forbidden emission lines are also detected in both bands. These *H*-band [Fe II] and *K*-band H_2 lines are commonly observed in outflows and HH objects. However, the $^2P \rightarrow {}^4P$ [Fe II] lines in the *K*-band are more difficult to detect (Takami et al. 2006), since they originate from Fe^+ levels with energies of about 2.6×10^6 K, more than twice as high as the upper energy levels of the *J*-band [Fe II] lines associated with the $^4D \rightarrow {}^4F$ transitions (the level energy of the 1.644 μm line is at 1.1×10^6 K). Obviously the longer wavelength lines suffer less from extinction effects, and may therefore be excellent probes of the ionised jet component close to the central source (Takami et al. 2006). The 2.244 μm $^2P_{3/2} \rightarrow {}^4P_{1/2}$ line is

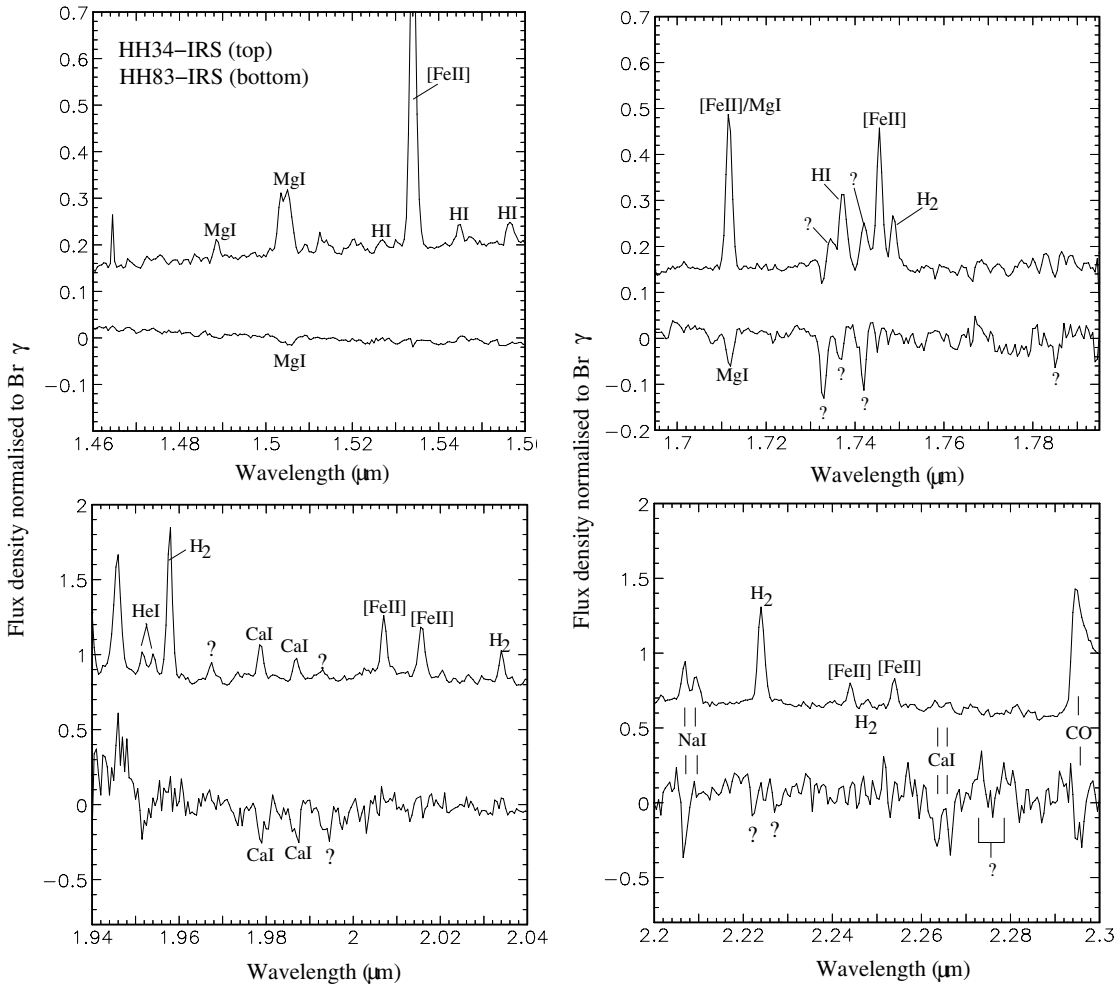

Fig. 7. A comparison of *H* and *K*-band spectral segments for HH 34-IRS and HH 83-IRS. The HH 34-IRS spectra have been shifted vertically.

detected in our HH 34-IRS data (see Fig. 7) and possibly also towards HH 72-IRS.

If CO and the various atomic permitted lines are associated with circumstellar matter and, specifically, an accretion disk, one might expect to see a correlation between these lines. Antoniucci et al. (2008) have already shown that the Na I doublet at 2.21 μm correlates with CO 2–0 bandhead emission. In the six sources with Na I and CO emission in our sample we identify a similar correlation (Fig. 8). For the modest set of data in this figure we measure a correlation coefficient, r, of 0.984; this corresponds to a probability, P, of only 2% that a random distribution of data points could produce the observed correlation (see Table 5).

A correlation is also seen between CO and the sum of the Ca I 1.987 μm and Ca I 1.978 μm lines ($r \sim 0.95$); the relationship between CO and the Mg I doublet at 1.50 μm is less clear, although interestingly the two outliers in the bottom panel in Fig. 8 – HH 34-IRS and SVS 13 – are the two sources with potentially the least extinction (discussed further below). These two objects may be marginally more evolved than HH 300-IRS, HH 72-IRS, HH 999-IRS and HH 26-IRS, or they may be orientated such that the Mg I/CO intensity ratio is enhanced.

We also consider whether tracers of accretion correlate with tracers of outflow. Accretion-signature lines are not always associated with jet signature lines (Doppmann et al. 2005; Nisini et al. 2005; Antoniucci et al. 2008). In TTSs, for example, CO, Na I, Mg I etc. are observed in absorption

Table 5. Linear-correlation analysis for the plots in Figs. 8 and 9.

Ratio	r^a	P^b
Na I-CO	0.984	2%
Ca I-CO	0.946	7%
Mg I-CO	0.866	17%
H_2-CO	0.826	21%
[Fe II]-CO	0.341	59%

Notes. [(a)] Linear-correlation coefficient, r, between the log-log values of the line intensities plotted in Figs. 8 and 9. Zero corresponds to no correlation, unity to complete correlation. [(b)] Probability, P, that a random sample of measured line intensities could produce a linear-correlation coefficient, r, equal to the value listed in the second column (Bevington & Robinson 1992). P should be less than a few percent if a correlation exists between the measured line intensities.

(Doppmann et al. 2005). Indeed, in our HH 83-IRS spectra there is a hint of CO in absorption; the atomic lines are also seen in absorption. In Fig. 9 we plot H_2 and [Fe II] line intensities against the sum of the first two CO bandheads. Clearly there is no correlation between these lines (high values of P are listed in Table 5). Presumably this is due to the variable nature of accretion and outflow activity in young stars, and the influence the ambient medium has on the observed intensities of emission lines

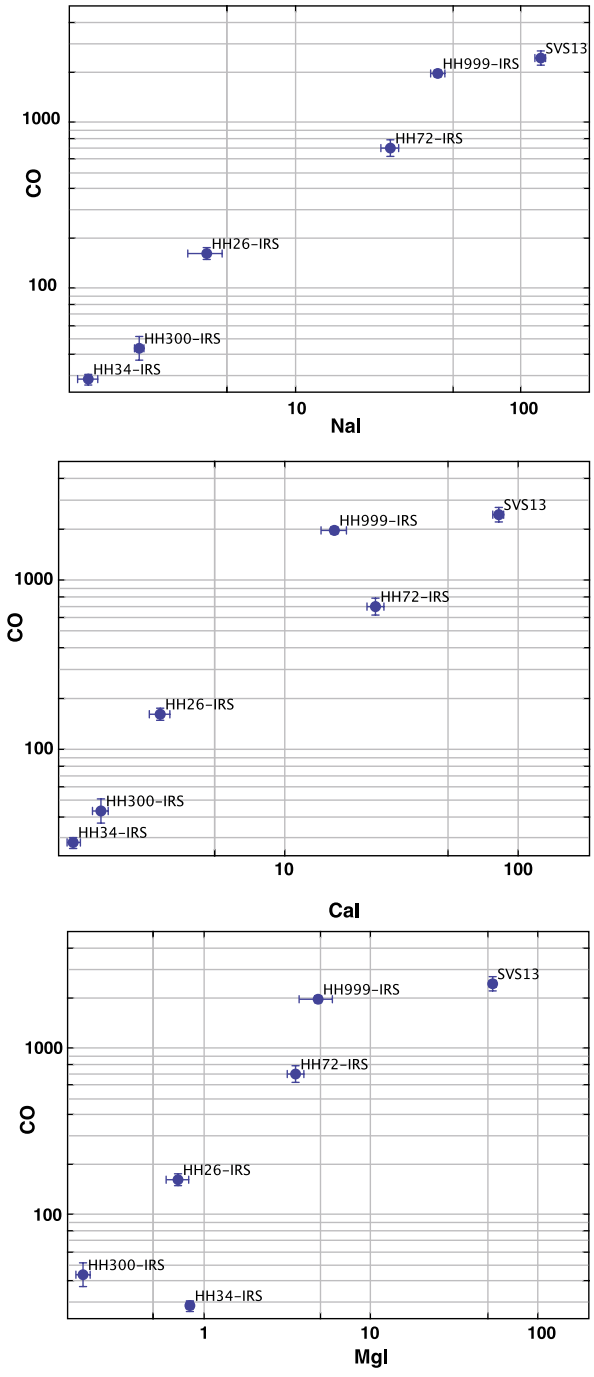

Fig. 8. Plots of atomic line-doublet intensities against the sum of the CO 2–0 and 3–1 bandhead intensities (in units of 10^{-17} W m^{-2}); *top* – Na I 2.207 μm+2.209 μm, *middle* – Ca I 1.978 μm + 1.987 μm, *bottom* – Mg I 1.503 μm + 1.505 μm.

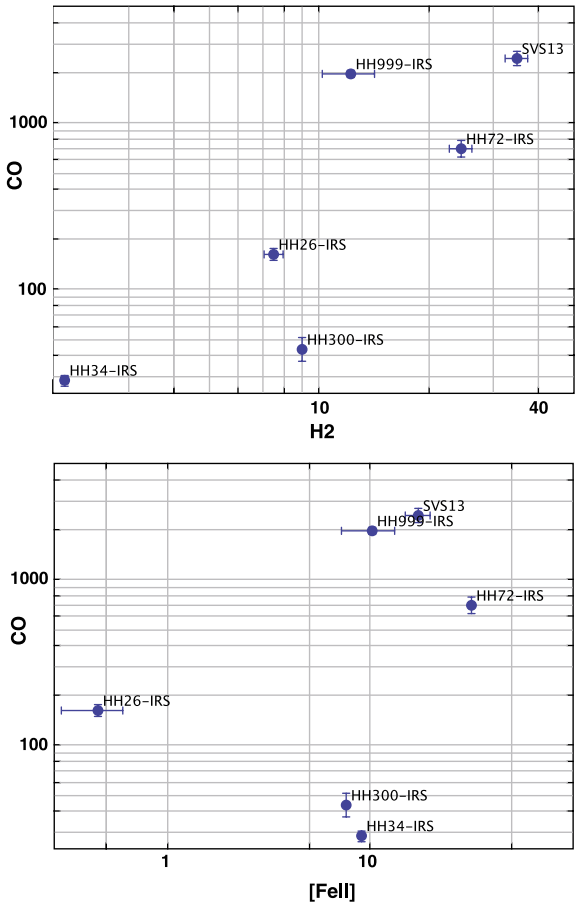

Fig. 9. Plots of the H_2 1–0 S(1) (*top*) and [Fe II] 1.644 μm (*bottom*) intensities against the sum of the CO 2–0 and 3–1 bandhead intensities (in units of 10^{-17} W m^{-2}).

in outflow shocks. We also stress that we have observed only a small number of objects.

Finally, Doppmann et al. (2005) propose that Class I sources, selected based on broad-band photometry, span a range of circumstellar properties, from heavily accreting to relatively quiescent. In high signal-to-noise Keck spectroscopy of 52 Class I and flat-spectrum sources, they find that only 15% exhibit CO emission or absorption; in our more modest sample of protostars, selected because of their association with molecular outflows, all exhibit CO emission bar one, the most evolved source in our sample, HH 83-IRS. This certainly suggests that outflow activity is a useful tracer of youth.

3.4. Extinction

Analysis of the conditions at the base of each jet ideally requires knowledge of the extinction, A_V. Towards an embedded young star A_V can be estimated from a near-infrared (near-IR) colour–colour diagram, provided the source lies close to the reddening band associated with the main sequence dwarfs and giants. In Fig. 10 we plot the 2MASS colours of our seven sources. All lie to the right of the reddening band, in the part of the diagram usually occupied by T Tauri stars and embedded Class I protostars (Lada & Adams 1992; Meyer et al. 1997). On face value, SVS 13 and HH 34-IRS appear to be less extincted than the other five sources, which cluster together near the top of the diagram and exhibit relatively extreme $J - H$, $H - K$s colours. The A_V values needed to de-redden each data point, i.e. move it on to the T Tauri locus, are listed in Table 6. These values should be viewed with some caution, however, since the classical T Tauri locus is defined for optically-visible Class II sources surrounded only by an accretion disk; detailed modeling of the infalling envelopes that surround the Class I sources in our study is required to take into account the affects the intrinsic excess and scattering associated with the envelope have on the $J - H$ and $H - K$s colours.

Table 6. Extinction towards each FEL/MHEL region. Line intensities/ratios are measured in a 0.5″ × 0.5″ aperture centred on each source.

Source	C–C[a] Diag A_v (mag)	H I ratio[b] 1.818/2.166 A_v (mag)	[Fe II] ratio[c] 1.600/1.712 A_v (mag)	[Fe II] ratio[c] 1.664/1.745 A_v (mag)	[Fe II] ratio[c] 1.644/1.810 A_v (mag)	H_2 ratio[d] 2.122/2.424 A_v (mag)	H_2 excitation[e] diagram A_v (mag)	Published[f] values A_v (mag)
HH 34-IRS	4 ± 1	6.3 ± 1	36 ± 8	16 ± 1	39 ± 2	35 ± 5	0–6	>7.1[1], 45[2], 412–32[3]
HH 300-IRS	22 ± 1	39 ± 4	*–ve*	...	61 ± 16	*–ve*	0–27	...
SVS 13	10 ± 1	9.7 ± 1	>128	...	<47	<80	...	6–15[3]
HH 72-IRS	10 ± 4	4.0 ± 1	51 ± 4	23 ± 2	42 ± 3	...	0	4.7[4]
HH 999-IRS	22 ± 3	8.2 ± 1	62 ± 21	...	...	...	...	...
HH 26-IRS	14 ± 2	...	>80	...	<54	38 ± 6	17–27	37[2]
HH 83-IRS	15 ± 2	...	...	...	...	...	...	...

Notes. [(a)] A_v estimates derived by de-reddening $J-H$, $H-K$s colours of each source in a near-IR colour–colour diagram (Fig. 10). [(b)] Extinction towards the H I recombination region at the base of each outflow, assuming case B recombination theory for $n_e = 10^9$ cm^{-3}, $T_e = 2000$ K (Hummer & Storey 1987): $A_v = -69.44 \times \log(1.25 \times [I_{(9-4)}/I_{Br\gamma}])$. [(c)] Extinction towards the FEL region at the jet base. Values are calculated from three pairs of lines: $A_v = -132 \times \log(0.262 \times [I_{1.600}/I_{1.712}])$, $A_v = -208 \times \log(0.499 \times [I_{1.664}/I_{1.745}])$, and $A_v = -104 \times \log(0.201 \times [I_{1.644}/I_{1.810}])$. [(d)] Extinction towards the H_2 emission line (MHEL) region associated with each jet, derived from the ratio of the 1–0 S(1) and 1–0 Q(3) lines: $A_v = -114 \times \log(0.704 \times [I_{S1}/I_{Q3}])$. [(e)] Range of extinction values towards the MHEL region, derived by minimising the scatter of data points in H_2 excitation diagrams; see Appendix C for details. [(f)] Extinction estimates taken from the literature; the superscript refers to the following publications: 1. Podio et al. (2006); 2. Antoniucci et al. (2008); 3. Takami et al. (2006); 4. Giannini et al. (2004) (measured only in the extended molecular outflow).

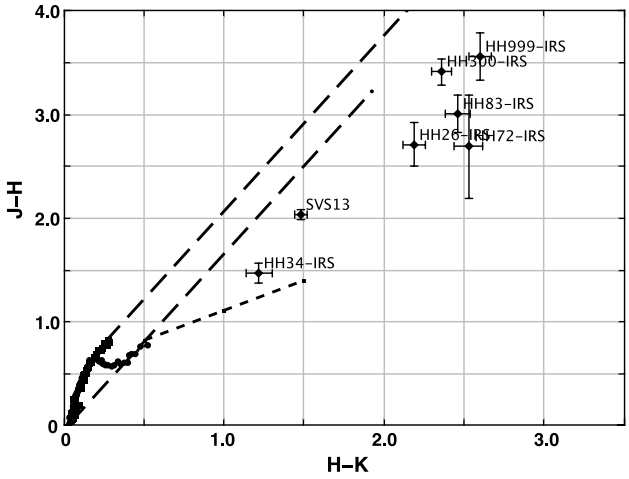

Fig. 10. Near-IR colour–colour diagram based on 2MASS magnitudes. The thick black dots lower-left mark the locus of intrinsic colours for main sequence dwarfs and giants (Koorneef 1983); the two long-dashed parallel lines are reddening vectors for the main sequence stars up to $A_v = 30$ mag (Rieke & Lebofsky 1985); the short-dashed line indicates the locus of T Tauri stars (Meyer et al. 1997).

The extinction toward the MHEL/FEL regions can be estimated from pairs of emission lines well separated in wavelength, provided the lines share the same upper energy level.

– H_2 Q-branch lines (Q(3), Q(4) and Q(5)) can be used with the 1–0S(1), S(2) or S(3) transitions (e.g. Gredel 1992; Giannini et al. 2004; Takami et al. 2006; Beck 2007). The 1–0S(1)/1–0Q(3) ratio is most commonly used in studies of HH objects and extended molecular outflows; we therefore use this ratio in Table 6. We adopt the transition probabilities of Wolniewicz et al. (1998) and assume an extinction law of the form $A_\lambda/A_v = (\lambda_v/\lambda)^{1.6}$ (where $\lambda_v = 0.55$ μm, Rieke & Lebofsky 1985). However, one should note that the Q-branch lines appear in a region of poor atmospheric transmission ($\lambda > 2.4\,\mu$m); towards accreting protostars these lines may also be superimposed on top of CO bandhead emission (see for example Fig. 6).
– [Fe II] transitions can also be used to evaluate A_v, though typically pairs of lines in the J and H-bands, well separated in wavelength, are utilised (e.g. [Fe II]1.64 μm/1.25 μm or [Fe II]1.64 μm/1.32 μm, Podio et al. 2006). We do not have access to J-band data. We therefore pair 1.600 μm with 1.712 μm ($a^4D_{3/2} \rightarrow a^4F_{7/2}$ with $a^4D_{3/2} \rightarrow a^4F_{5/2}$), 1.664 μm with 1.745 μm ($a^4D_{1/2} \rightarrow a^4F_{5/2}$ with $a^4D_{1/2} \rightarrow a^4F_{3/2}$), and 1.644 μm with 1.810 μm ($a^4D_{7/2} \rightarrow a^4F_{9/2}$ with $a^4D_{7/2} \rightarrow a^4F_{7/2}$). We use the extinction law quoted above and, in Table 6, quote values for A_v from these three sets of line ratios. We adopt the transition probabilities of Nussbaumer & Storey (1988). Like Takami et al. (2006) we find that A_v values derived from the 1.664 μm/1.745 μm ratio are lower than those obtained from the other two [Fe II] ratios and, in the case of HH 34-IRS, the H_2 ratio.
– H I Brackett line ratios can be compared to theoretical values to estimate the extinction towards the hydrogen recombination zone. Hummer & Storey (1987) compute the relative intensities for H I recombination lines for a range of temperatures (500 K $\leq T_e \leq$ 30 000 K) and electron densities (100 cm$^{-3} \leq n_e \leq 10^{14}$ cm^{-3}). Recently, Bary et al. (2008) have shown that the Brackett decrement in active T Tauri stars is consistent with case B recombination theory at high densities though relatively low temperatures ($n_e \sim 10^9$–10^{10} cm^{-3}, $T_e \leq 2000$ K). Under these conditions the two strongest Brackett lines in the H and K-bands, H I(9–4) and Brγ (H I(7–4)), have a ratio of 0.65–0.94 (Hummer & Storey 1987). In Table 6 we quote extinction values based on a ratio of 0.80. Lower ratios consistent with lower densities and higher temperatures (H I(9–4)/Brγ = 0.46 for $n_e \sim 10^6$ cm^{-3}, $T_e \sim 3000$ K) ultimately produce unphysical, negative values for the extinction. The positive values listed in Table 6 imply that the conditions used by Bary et al. for T Tauri stars are also appropriate for the younger Class I sources analysed here. Note, however, that the 9–4 transition is again close to the edge of the H-band atmospheric window and so is potentially difficult to measure accurately.

Reducing the scatter of data points plotted in H_2 excitation diagrams is another possible technique for measuring A_v, provided sufficient ro-vibrational lines are detected (Nisini et al. 2002; Caratti o Garatti et al. 2006). If the gas is thermalised to a single excitation temperature, in a plot of $\ln(N_{v,J}/g)$ (where $N_{v,J}$ is the column density of the v, J ro-vibrational level and g is the statistical weight) against upper-level energy, $E_{v,J}$, the points should lie on a straight line. For the range of temperatures expected in a post-shock cooling zone, a curve is often a better fit to the data. In either case, correcting the column densities for extinction should reduce the scatter of data points about a linear or polynomial fit. Varying A_v and analysing the goodness-of-fit should then lead to an estimate of the extinction. We describe this process in detail in Appendix C, and include the range of extinction values measured in this way towards our outflow sources in Table 6.

None of the above techniques can be viewed as entirely satisfactory. Although measured in the same $0.5'' \times 0.5''$ aperture, the line ratios listed in Table 6 trace different regions in each system; the Brackett lines almost certainly originate from a region very close to the central object, while the H_2 and [Fe II] lines trace a more extended region along the jet axis. One might expect the extinction values derived from the former to be generally higher, though also sensitive to the orientation of the system (an edge-on disk resulting in increased A_v towards the central source). Each method also assumes that line intensities are modified only by line-of-sight extinction and that the standard ISM extinction law is valid. None of the methods take into account the effects of scattering, which increase the observed intensities of the shorter-wavelength transitions (causing, for example, JHK colours to be "bluer"). Scattering will almost certainly be important in these dense regions. The [Fe II] lines are also relatively close in wavelength; these ratios are less sensitive to extinction than lines that are more widely spaced spectrally.

In her study of Class I and flat-spectrum YSOs, Beck (2007) measures a wide range in extinction when comparing A_v values derived from H I Brα/Brγ and H_2 ratios with values calculated from spectral synthesis models, the column density of water ice observed in her spectra, and by de-reddening $J - H$ and $H - K$ colours in colour–colour diagrams. Beck notes that future detailed modeling of scattered light images and SEDs may result in more robust A_v measurements. Of the methods considered by Takami et al. (2006), the 1–0 S(1)/1–0Q(3) ratio was preferred, since it often agrees with values based on S(0)/Q(2) and S(2)/Q(4) ratios. Takami et al. also consider values derived from the [Fe II] 1.600 μm/1.712 μm ratio to be upper limits; we likewise find these values to be on the high side.

In conclusion, we consider the [Fe II] 1.644 μm/1.810 μm ratio, the H_2 2.122 μm/2.424 μm ratio, and the H_2 excitation diagram analysis to be the more reliable spectroscopic techniques for estimating the extinction. The values derived from linear fits to H_2 line intensities in the excitation diagrams in Appendix C seem to be too low in some sources; a polynomial fit is preferred. With the possible exception of HH 72-IRS, the extinction values measured for our sample of outflow sources are consistent with values found in the literature, which we also list in Table 6.

In Fig. 11 we plot images of the extinction at the base of each outflow, derived from the ratio of the 1–0 S(1) and 1–0 Q(3) H_2 lines, and the 1.644 μm and 1.810 μm [Fe II] transitions (the H I recombination line emission is not extended so similar plots in H I(9–4)/(7–4) have not been produced). The plot of extinction in each panel is confined to regions where line emission (in the weakest transition) is detected. Even so, we see that in almost all cases the extinction is highest towards the source continuum

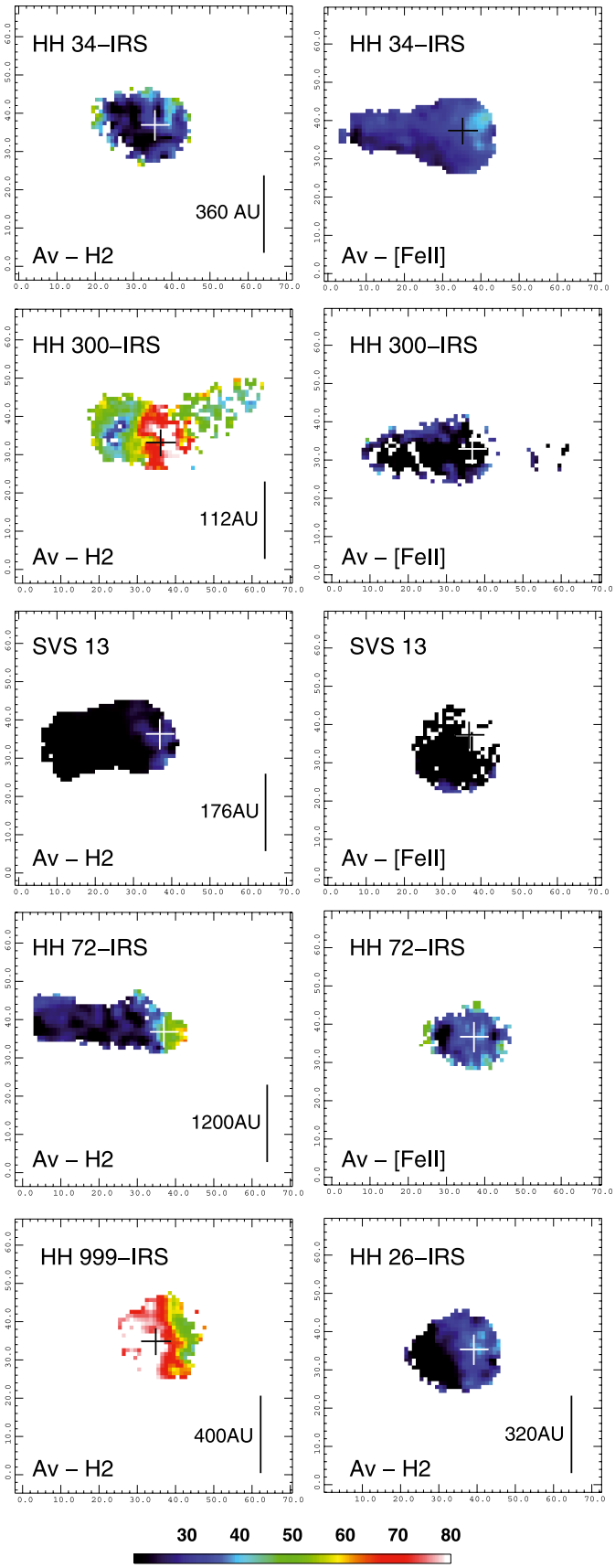

Fig. 11. Images showing the distribution of extinction, A_v, derived from the H_2 1–0 S(1)/1–0 Q(3) and the [Fe II] 1.644/1.810 μm line ratios. Regions with no emission above the 2σ noise level in either line have been masked; crosses mark the continuum peak position; the scale bars all measure $0.8''$.

Table 7. Electron densities based on [Fe II] line ratios (uncorrected for extinction) measured in a 0.5″× 0.5″ aperture centred on each source.

Source	[Fe II] ratio 1.533/1.644	n_e (cm^{-3})	[Fe II] ratio 1.600/1.644	n_e (cm^{-3})	[Fe II] ratio 1.664/1.644	n_e (cm^{-3})	[Fe II] ratio 1.677/1.644	n_e (cm^{-3})
HH 34-IRS	0.24 ± 0.02	$\geq 3 \times 10^4$	0.22 ± 0.01	$\sim 3 \times 10^4$	0.15 ± 0.01	$\sim 1 \times 10^5$	0.29 ± 0.02	$\geq 1 \times 10^5$
HH 300-IRS	0.25 ± 0.06	$\geq 3 \times 10^4$	0.23 ± 0.03	$\sim 3 \times 10^4$	0.16 ± 0.09	$\sim 1 \times 10^5$	0.68 ± 0.13	$\geq 1 \times 10^5$
SVS 13	0.67 ± 0.21	?	<0.57	?	<0.3	?	<0.3	$\leq 1 \times 10^5$
HH 72-IRS	0.20 ± 0.01	$\sim 1 \times 10^4$	0.25 ± 0.02	$\geq 4 \times 10^4$	0.18 ± 0.01	$\geq 1 \times 10^5$	0.33 ± 0.04	$\geq 1 \times 10^5$
HH 999-IRS	0.10 ± 0.03	$\sim 1 \times 10^3$	0.30 ± 0.12	$\geq 1 \times 10^5$	<1.0	?	<0.12	$\leq 1 \times 10^4$
HH 26-IRS	<0.23	$\leq 2 \times 10^4$	<1.0	?	<0.3	?	<0.3	$\leq 1 \times 10^5$

position, decreasing sharply along the flow axis. The extinction as measured from H_2 and [Fe II] is relatively consistent in each source; only in HH 300-IRS do we see a large difference, A_v being considerably higher in the H_2 data.

3.5. Electron density at the base of each jet

[Fe II] is a useful tracer of the electron density, n_e, and electron temperature, T_e, in the ionised jet component at the base of each outflow (Nisini et al. 2002). When measuring n_e the 1.533 μm/1.644 μm line ratio is the least sensitive to electron temperature, although the 1.600 μm/1.644 μm, 1.664 μm/1.644 μm and 1.677 μm/1.644 μm ratios are expected to provide more accurate densities because of the limited effects of extinction on these spectrally-adjacent transitions (Nisini et al. 2002; Takami et al. 2006; Podio et al. 2006; Garcia Lopez et al. 2008; Giannini et al. 2008). At densities above 10^5 cm^{-3} and for temperatures in the range 5000–20 000 K, these ratios saturate at thermalised values of: 1.533 μm/1.644 μm = 0.37–0.41, 1.600 μm/1.644 μm = 0.29–0.34, 1.664 μm/1.644 μm = 0.15–0.19, and 1.677 μm/1.644 μm = 0.27–0.30.

In Table 7 we list these line ratios and, using the models of Nisini et al. (2002) and Takami et al. (2006), predict the electron density at the base of each outflow. The 1.664 μm/1.644 μm and 1.677 μm/1.644 μm ratios yield somewhat higher values for n_e than the other two ratios. The 1.664 μm line is the weakest of the four considered here, and is only reliably detected in HH 34-IRS; the 1.677 μm line is blended with H I (11–4) at 1.681 μm and so is also arguably less reliable. Even so, for SVS 13 and HH 34-IRS our measurements are generally consistent with the higher-spectral-resolution Subaru Telescope observations of Takami et al. (2006, the areas they label "Region 1" in their position-velocity diagrams are roughly consistent with our IFS field-of-view). Notably, the high 1.533 μm/1.644 μm ratio and even the large 1.600 μm/1.644 μm upper limit in Table 7 for SVS 13 are also observed by Takami et al. Both are unphysically high. Correcting for extinction would *increase* both line ratios so this cannot account for these high values. In some sources the 1.533 μm/1.644 μm could be affected by contamination of the [Fe II] 1.533 μm line intensity by H I (18–4) at 1.535 μm, although this seems unlikely for HH 300-IRS and HH72-IRS where the [Fe II]/Brγ ratio is high (note also that Takami et al. resolve these two lines and find H I (18–4) contamination to be negligible). In any case, all three line ratios indicate an electron density of the order of 10^4–10^5 cm^{-3} at the base of each outflow.

In Figs. 12 and 13 we present images of HH 34-IRS, HH 300-IRS and HH 72-IRS in each line ratio. These three sources are the brightest [Fe II] emitters in our sample of targets. The images have not been corrected for extinction because of the uncertainties associated with A_v (discussed earlier) and because the lines are in any case very close in wavelength. Figure 12 clearly illustrates a decrease in line ratio – and therefore a decrease in gas density – with distance from the HH 34-IRS source along the jet axis (i.e. towards the left). This decrease is evident in three of the four ratio diagrams and therefore can not be an effect of extinction (a sharp decrease in electron density along the HH 34 jet has also been reported by Podio et al. 2006; and Garcia Lopez et al. 2008). The 1.664 μm/1.644 μm ratio appears relatively constant along the jet axis, though again we stress that the 1.664 μm line is the weakest of the four used here. The 1.677 μm/1.644 μm ratio is also noticeably high towards the jet driving source in panel (d) (towards the centre of the image), as noted earlier. We do not observe a decrease in density across the width of the flow (i.e. higher density along the flow axis; lower towards the flow edges), although this is probably because the width of the flow is unresolved.

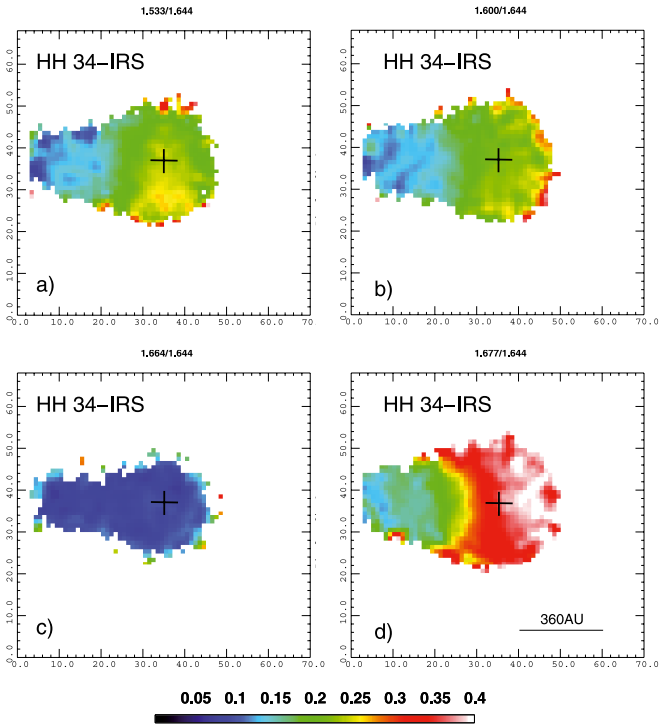

Fig. 12. Images of HH 34-IRS showing [Fe II] line ratios that are sensitive to the electron density. Ratios are: **a)** 1.533 μm/1.644 μm; **b)** 1.600 μm/1.644 μm; **c)** 1.664 μm/1.644 μm and **d)** 1.677 μm/1.644 μm. Regions with no line emission above the 3σ noise level in regions of blank sky have been masked. The cross in each panel marks the *H*-band continuum peak position; the scale bar again corresponds to 0.8″.

Table 8. Mass outflow rate and momentum flux in the H_2 and [Fe II] flow components.

Source	$I_{[FeII]}{}^a$ (W m^{-2})	$I_{H2S(1)}{}^a$ (W m^{-2})	$A_v{}^b$ (mag)	$V_{[FeII]}{}^c$ (km s^{-1})	$V_{H2}{}^c$ (km s^{-1})	$\dot{M}_{[FeII]}{}^d$ ($M_\odot$ yr^{-1})	$\dot{M}_{H2}{}^d$ ($M_\odot$ yr^{-1})	$\dot{M}V_{[FeII]}{}^d$ ($M_\odot$ km s^{-1})	$\dot{M}V_{H2}{}^d$ ($M_\odot$ km s^{-1})
HH 34-IRS	2.0×10^{-16}	6.9×10^{-17}	31	103	7	2.7×10^{-5}	2.3×10^{-7}	7.5×10^{-3}	4.2×10^{-6}
HH 300-IRS	2.3×10^{-17}	3.9×10^{-17}	44	133	5	8.4×10^{-6}	4.3×10^{-8}	2.2×10^{-3}	4.3×10^{-7}
SVS 13	4.5×10^{-16}	2.0×10^{-15}	10	141	28	1.4×10^{-6}	2.4×10^{-7}	2.5×10^{-4}	8.6×10^{-6}
HH 72-IRS	4.6×10^{-16}	4.1×10^{-16}	39	150	60–149	1.4×10^{-3}	$1.6–3.9 \times 10^{-5}$	2.9×10^{-1}	$1.3–8.2 \times 10^{-3}$
HH 999-IRS	7.3×10^{-17}	3.3×10^{-16}	22	100*	10*	2.7×10^{-6}	2.8×10^{-7}	3.9×10^{-4}	3.9×10^{-6}
HH 26-IRS	...	3.1×10^{-16}	30	...	56	...	6.5×10^{-6}	...	8.7×10^{-4}

Notes. [a] Integrated line intensities measured from the images presented in Fig. 2. $I_{[FeII]}$ and $I_{H2S(1)}$ are *not* corrected for extinction. Intensities are integrated across the entire extent of the observed jet in each object. [b] Extinction, A_v. For each source the median of values measured from H_2 and [Fe II] line ratios and/or H_2 rotational excitation diagrams (listed in Table 6) is used. If these are not available, the extinction measured from the colour–colour diagram is employed. [c] H_2 and [Fe II] flow component radial velocities, uncorrected for flow orientation (see Table 2 in Davis et al. 2003, for details). Two equally strong peaks are detected in the H_2 echelle spectrum of HH 72-IRS – the range in values above takes into account these two velocities. For HH 999-IRS we use canonical values, based on the other sources in this table (data are marked with a *); the HH 26-IRS H_2 velocity is taken from Antoniucci et al. (2008). [d] Mass outflow rate and momentum flux in each flow component, derived using the velocities list in Cols. 5 and 6, corrected for the flow orientation angle listed in Tables 2 and 3. All values are also corrected for the extinction, A_v, listed in Col. 4 above.

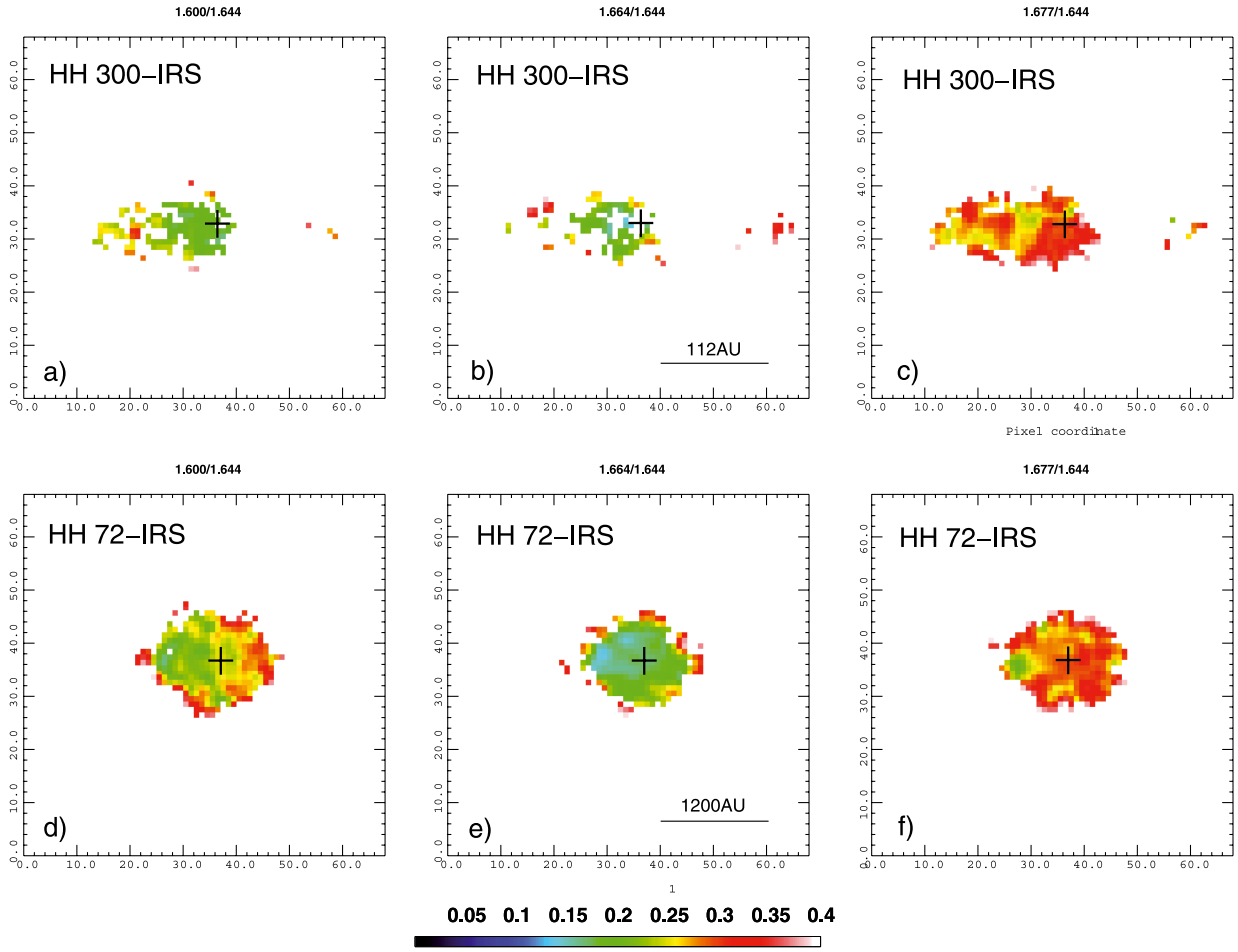

Fig. 13. Images showing [Fe II] line ratios that are sensitive to the electron density, for HH 300-IRS **a)–c)** and HH 72-IRS **d)–f)**. 1.600 μm/1.644 μm, 1.664 μm/1.644 μm and 1.677 μm/1.644 μm ratios are shown for each source. Regions with no line emission have again been masked. The crosses mark the *H*-band continuum peak position in each image; the scale bars measure 0.8″.

Towards HH 300-IRS the [Fe II] emission is extended along the flow axis (see Fig. 2), though it is also much weaker than in HH 34-IRS. Consequently, density gradients are more difficult to see in this outflow. Even so, there is perhaps a hint of a gradient in the 1.677 μm/1.644 μm image (Fig. 13c). In this figure the ratio is high in the centre, though marginally lower towards the left. HH 72-IRS is the most distant source in our sample; the outflow lobes are weak in [Fe II] emission and the weaker [Fe II] lines are observed only towards the outflow source position (the emission is slightly extended along the flow axis, i.e. left-right).

3.6. Mass loss rate and momentum flux in the H_2 and [Fe II] flow components

Our continuum-subtracted H_2 and [Fe II] images allow us to measure the mass loss rate and momentum flux at the base of each outflow in each flow component. From the images in Fig. 2 we measure the integrated intensity across the entire flow observed in our IFS data. The area associated with these MHEL/FEL flow components is assumed to be equal to the extent of the flow along the jet axis (measured from the profiles in Fig. 3 where the intensity drops to 50% of the nearest peak), multiplied by the width of the flow (which in all cases is effectively the seeing). We correct these integrated intensities for extinction, using an estimate based on the ranges of A_v values derived from the observed H_2 and [Fe II] line ratios and/or H_2 excitation diagrams listed in Table 6. Following Davis et al. (2001, 2003), the column density of gas (in units of m^{-2}) is then given by:

$$N_{H2} = 2.76 \times 10^{28} \times I_{H_2} 10^{A_v/21.7} \times 4/(a\pi) \quad (1)$$

and

$$N_H = 7.03 \times 10^{28} \times I_{[FeII]} 10^{A_v/14.4} \times 4/(a\pi) \quad (2)$$

I_{H2} and $I_{[FeII]}$ are in units of W m^{-2}. a is the area of each flow component in steradians. Multiplying each column density by this area (in m^{-2}) and by the mass of molecular hydrogen (atomic hydrogen for the [Fe II] component) gives the total mass of the flow component.

The orientation angle of each MHEL/FEL jet with respect to the line of sight, α, was obtained from the literature (Chrysostomou et al. 2000; Davis et al. 2003, and references therein); the values used are listed in Tables 2 and 3. For each flow component velocity we use the peak radial velocity measured in the echelle spectroscopic observations of Davis et al. (2001, 2003; see also Takami et al. 2006); note that HH 300-IRS corresponds to IRAS 04239+2436 in these earlier studies. HH 26-IRS and HH 999-IRS were not observed by Davis et al; we therefore adopt "typical" values for $V_{[FeII]}$ and V_{H2}, based on the other sources listed in Table 8, for HH 999-IRS, and use the (unusually high) radial velocity measured by Antoniucci et al. (2008) for HH 26-IRS.

Mass loss rates and momentum fluxes, based on these velocities and the length of the observed MHEL/FEL jet, are listed in Table 8. Values derived for the [Fe II] flow component should be regarded as lower limits, due to the unknown [Fe II] depletion factor (Nisini et al. 2005; Podio et al. 2006); the fraction of Fe that is single ionised is also a source of uncertainty (Hamann et al. 1994). The dominant sources of error are the extinction and flow velocity. The lowest value of A_v used is 10 mag, the highest 44 mag. 34 mag of extinction is equivalent to a factor of ~20 difference in the H_2 data, and a factor of ~500 difference in the shorter-wavelength [Fe II] results. The velocities used should be relatively reliable, since these have been directly measured in most of our targets. However, note that if multiple velocity components have been observed, only the highest-velocity is used (see Davis et al. 2003, for details). Flow orientation angles are probably accurate to within 10–20° in most of our targets; an increase in angle from 40° to 60° increases $\dot{M}$ and $\dot{M}V$ by a factor of only 2–3, so α is probably a secondary source of error.

Based on optical and near-IR spectroscopic studies over multiple knots along the well-known jets HH 111, HH 34 and HH 83, Podio et al. (2006) measure mass fluxes of the order of 10^{-7}–10^{-8} $M_\odot\,yr^{-1}$; similar values are reported for HH 1 and HH 34 by Garcia-Lopez et al. (2008), for the DG Tau jet by Agra-Amboage et al. (2009), and from optical spectroscopy of HH jets by Bacciotti & Eislöffel (1999). Closer to the central engine, Davis et al. (2001, 2003) measure $\dot{M}$ from their H_2 and [Fe II] echelle spectroscopic data; $\dot{M}$ is measured to be marginally higher in these inner jet regions, in the range 10^{-6}–10^{-8} $M_\odot\,yr^{-1}$. Higher mass loss rates might be expected close to the source if further downstream the jet sweeps up and entrains cold ambient material (a "CO outflow", for example), since mass loading of this form would require the transfer of momentum from the hot atomic/molecular jet observed in [Fe II] and H_2. However, Antoniucci et al. (2008) have observed some of the same outflow sources and measure mass loss rates more consistent with the larger-scale studies, with $\dot{M}$ again in the range 10^{-7}–10^{-8} $M_\odot\,yr^{-1}$.

The $\dot{M}$ and $\dot{M}V$ values reported here in Table 8 are in general consistent with or higher than these earlier studies. Larger values could result from the use of higher extinction values. We have already demonstrated that A_v drops off sharply with distance from each source, so the values used in Table 8 may be high. Also, other studies have relied upon long-slit spectroscopic observations which miss the off-axis emission included in the current 3-D dataset. Since the mass loss rate is based on a dynamical time scale measured only from the "length" of the MHEL/FEL jet, this additional mass would result in higher mass-loss and momentum flux estimates.

The momentum supply rate or momentum flux, $\dot{M}V$, is often reported to be higher in [Fe II] than in H_2 (e.g. Davis et al. 2003; Podio et al. 2006; Agra-Amboage et al. 2009). To some extent this is not too surprising, given the order-of-magnitude greater velocities observed in [Fe II] over H_2. High values of A_v will also enhance the $\dot{M}V_{[FeII]}/\dot{M}V_{H2}$ ratio. Even so, the results in Table 8 do suggest that the atomic "jet" component certainly could supply sufficient momentum to drive the molecular flow component. The molecular outflow, observed in H_2 emission in each of our six Class I sources, may therefore be "jet driven".

4. Discussion

4.1. H_2 and [Fe II] as tracers of jets from young stars

Our high spatial resolution IFS observations of seven young stars demonstrate the abundance of diagnostic lines available in the near-infrared. These lines probe both accretion and outflow processes. The 3-D IFS observations yield excitation data and line ratios, as well as spatial information on AU scales, data that are complementary to echelle spectroscopy studies which provide kinematic information for each emission line.

Previous excitation and kinematic studies of MHEL regions associated with a handful of Class I protostars suggest that the H_2 ro-vibrational emission in the H and K-bands derives from shock-heated gas at temperatures of ~2000–3000 K and with densities of 10^5–10^6 cm^{-3} if H–H_2 collisions dominate, or 10^7–10^8 cm^{-3} if the gas is entirely molecular (Takami et al. 2006, note that H–H_2 collisional rate coefficients are ~100-times higher than H_2–H_2 rates; see also Giannini et al. 2002). Recent studies of classical T Tauri stars likewise reveal weak molecular line emission from the bases of associated HH jets (Beck et al. 2008, 2010; Agra-Amboage et al. 2009). The emission from these Class II YSOs is spatially extended (over a few hundred AU) and exhibits kinematic and excitation characteristics similar to those seen in the Class I jet sources discussed here. UV or X-ray heating is not thought to be a dominant source of excitation in either the Class I or Class II MHEL regions (Takami et al. 2004); rather, the emission must be associated

with shocks formed along the jet beam. Excitation in a boundary layer between the jet and the ambient medium seems unlikely since jets from young stars are known to be hypersonic (i.e. high Mach numbers). Such a jet is expected to have relatively little interaction with the surrounding environment; a massive *entrained* molecular flow component, within a few hundred AU of the central engine, is therefore unlikely (Ray 2000). The fact that the [Fe II] and H_2 flow component widths are comparable in most of our sources is certainly consistent with this interpretation.

The H_2 and [Fe II] emission profiles plotted in Fig. 3 illustrate two important aspects of FEL/MHEL regions: (i) the existence of sharp peaks, in both H_2 and [Fe II] emission, that are offset by a few tens to a few hundred AU along the jet axis, and (ii) the rapid decline in line intensity along the flow axis. The H_2 and [Fe II] peaks may be associated with the same discrete shock front – possibly a collimation shock at the Alfvén radius; the relative offsets between the H_2 and [Fe II] peaks and the different velocities reported in the literature for each flow component may be due to excitation in different parts of a non-planar (bow shaped or hemispherical) shock front. The rapid decrease in line intensity downwind of this shock front is more likely to result from radiative cooling than to a decrease in gas density. The dynamical time scales associated with the first few hundred AU of the jet amount to a few tens of years (e.g. 500 AU/100 km s^{-1} ~ 24 yrs); time scales may be longer for the slower molecular gas component. Radiative cooling times are hard to estimate, since the gas density and flow cross section will change rapidly as the flow advances and expands. However, they are likely to be a few years at most (note that HH objects and H_2 jets are known to vary in brightness and morphology on these sorts of time scales), considerably shorter than the dynamical time-scales. Detailed jet modeling is required to shed further light on this issue.

In T Tauri stars, optical HST observations have shown that the electron density is high at the jet base, rapidly declining along the flow within the first ~200–300 AU (e.g. Bacciotti & Eislöffel 1999). This behaviour is consistent with Magnetohydrodynamic (MHD) models in which the electron density is expected to decrease as the gas expands before being compressed again by internal shocks. A similar trend is seen in our [Fe II] observations for at least one Class I outflow, HH 34-IRS. [Fe II] is detected towards most of the other sources in our sample; deeper observations are required to establish whether the same rapid decrease in electron density applies along these other jets.

Gradients in jet density may of course be related to the broad flow opening angles reported in Table 4; an opening angle of the order of 20°–40° is inferred for most of the H_2 and [Fe II] flow components discussed in this paper. As noted earlier, similar opening angles have been observed in studies of HH jets from T Tauri stars – when these observations sample the same distance range along the jet axis (hundreds of AU) considered here. Although higher spatial resolution observations of Class I outflows are certainly warranted, our data are none-the-less consistent with two things: that ionised and molecular jet components have similar opening angles, and that jet opening angles do not appreciable increase as a young star evolves from being an embedded Class I protostar to an optically-visible T Tauri star. *Jet opening angles – which remain essentially fixed – may therefore be established early in the evolutionary sequence of a young, low mass star.*

Although Class I and Class II jets seem to possess wide opening angles within their first few hundred AU, at greater distances from the source, both H_2 and [Fe II] flow components must be re-collimated. Jet widths from Class I and Class II sources, whether observed in optical or near-infrared forbidden emission lines ([S II], [Fe II], etc.) or near-IR H_2 ro-vibrational lines, retain a high degree of collimation over thousands of AU and sometimes even over parsec-scale distances. The same seems to apply to jets from the youngest protostars, the Class 0 sources. Sub-millimetre interferometric observations of outflows from a number of highly embedded young stars have revealed highly collimated molecular jets (e.g. Lee et al. 2008, 2010; Hirano et al. 2010). Cabrit et al. (2007) used the Plateau de Bure Interferometer to observe, in SiO emission at sub-arcsecond resolution, the collimated molecular jet associated with HH 212. They trace the jet to within 1000 AU of its driving source, a deeply embedded Class 0 source hidden from view even at near-IR wavelengths. Cabrit et al. find striking similarities between the HH 212 "microjet" and atomic jets from T Tauri stars. It seems clear that collimated molecular jets are a feature of outflows from Class 0, Class I and Class II young stars. Cabrit et al. also note that jet collimation occurs regardless of whether the source is enshrouded in a dense envelope or not; this fact alone appears to rule out jet collimation by external pressure, instead favouring a common MHD self-collimation process at all stages of low mass star formation.

4.2. Distinguishing between Jet Models – X-wind or Disk-wind?

One of the original goals of our SINFONI observations was to constrain jet collimation and acceleration models. The discussion in the previous section points to a relatively broad opening angle at the base of the jet, though this alone fails to distinguish between the X-wind and disk-wind models described in the introduction. In addition to a collimated jet, magneto-centrifugal X- and disk-wind models predict the existence of a low-velocity, wide-angled wind component (Shang et al. 2007; Pudritz et al 2007). Atomic and ionic lines from H I, [Fe II] and, at optical wavelengths, [O I] and [S II], require high densities and may therefore only be excited along the densest portions of a jet, very close to the jet axis. Molecular bipolar outflow morphologies often support the existence of wide-angled winds (Lee et al. 2000; Arce & Sargeant 2006). A relatively broad, low velocity molecular wind has also recently been detected surrounding the fast, HH jet from the young T Tauri star HL Tauri (Takami et al. 2007) and from the DG Tau jet (Beck et al. 2008).

The mere presence of excited H_2 emission at the base of each HH jet tends to support a disk-wind model (or at the very least a flow component that is ejected from large disk radii), since the conditions in the jet must permit the survival of H_2 and, at the same time, excite forbidden emission lines from ionised species such as S^+ and Fe^+. The bulk of the emission from an X-wind is produced in high-excitation on-axis material, whereas the outer streamlines of a disk-wind, where the flow originates from cooler, outer disk radii, may possess suitable conditions for H_2 excitation rather than H_2 dissociation.

Currently, the best way to distinguish between jet models is with detailed kinematic information, by measuring jet rotation (for X-winds the specific angular momentum is very low compared to the corresponding disk-wind models) and by analysing line profiles close to the central engine (X-wind theory predicts these to be rather narrow, whereas disk-wind theory suggests that they should be very broad, see e.g. Pyo et al. 2006; Cabrit 2009). With the current data set we do not have sufficient spectral resolution to comment on either of these issues.

With the SINFONI observation we have, however, established the *spatial characteristics* of the line emission regions associated with the base of each outflow. Although the observations are certainly affected by extinction, it is clear that any jet collimation and acceleration model must produce both H_2 and [Fe II] line emission which peaks close to – though not coincident with – the central object and then rapidly fades in intensity along the flow axis (if we exclude the distant source HH 72-IRS, then in both H_2 and [Fe II] we measure peak offsets along the flow axis in the range ∼10–200 AU, with the emission peaks extending over only 100–600 AU; see Tables 2 and 3). As mentioned earlier, these line emission features may be associated with collimation shocks formed at the Alfvén radius.

Obviously the objects considered in this paper are also ripe for further investigation at higher spatial and, particularly, higher spectral resolution.

4.3. Episodic accretion and outbursts

Finally, we mention that our source sample is potentially biased towards outbursting sources, since we have chosen our targets based on their association with known HH jets. Many of the emission lines observed in our data may be associated with, or enhanced by, recent outburst events. The diversity in jet characteristics, as traced in [Fe II] and H_2 emission, may also be a result of such non-steady outflow activity.

The CO bandheads are conspicuously strong in all of our Class I sources. CO is known to be variable in protostars; Lorenzetti et al. (2009) suggest that CO bandheads in EXor objects increase in intensity during outburst. Indeed, Aspin et al. (2010) have recently monitored significant changes in emission-line strengths over the period of ∼4 months in the prototype EXor, EX Lupi, while Biscaya et al. (1997) reported CO bandhead variability on time-scales as short as a few days in some low mass young stellar objects; in DG Tau, for example, the bands were observed to disappear and reappear.

CO has been monitored in one of our targets, SVS 13, by a number of groups. Eislöffel et al. (1991) compared their CO spectrum with earlier observations made by Carr (1989) and concluded that the equivalent width (EW) had not changed; Aspin & Sandell (1994) obtained four spectra spread over two years and also noticed no change in EW; Biscaya et al. (1997) monitored SVS 13 (referred to as SSV 13 in this paper) between 1995 and 1996 and generally obtained the same results. However, they did record a rapid flaring of the source continuum on one particular day – December 23, 1996 – that was not matched by a similar increase in CO intensity. Consequently, they measured a decrease in CO EW on this date by a factor of ∼2. Following Biscaya et al., we measure a line to continuum ratio, $R = F_{CO}/S_{2.3}$ of $13(\pm3) \times 10^{10}$ Hz (23(±5)Å), consistent with the range $12-18 \times 10^{10}$ Hz reported by Biscaya et al. when the source continuum was not flaring.

In surveys of young stars the CO bandheads at 2.3 μm are observed to be absent in some sources, and in absorption in others (e.g. Greene & Lada 1996; Reipurth & Aspin 1997). The presence of CO bandheads in all of our Class I sources is therefore somewhat unique, and may indicate that each source has undergone a recent accretion event. However, it seems unlikely that all were undergoing an EXor-type outburst coincidentally when we observed them. The bright CO bands in each of our sources must therefore be somewhat more constant phenomena than is observed in the more extreme EXor-type objects. Monitoring of Class I sources is certainly warranted, in CO but also in other "disk tracers" like Na I, Ca I and Mg I, if the origin of these nebular emission lines in these particularly young "pre-T Tauri-type" objects is to be revealed.

5. Concluding remarks

Near-IR emission lines are superb tracers of accretion and outflow processes at the bases of jets from Class I protostars. High spatial resolution IFS data may be used to illustrate the distribution of H_2 and [Fe II] in the MHEL and FEL regions in each source; profile fitting then leads to precise measurements of the extent and spatial offsets of these emission line features along each jet axis. In the *H* and *K*-band we also observe an abundance of atomic permitted lines, which presumably are collisionally excited in the outer regions of an accretion disk, while bright CO bandheads trace the dense inner regions of the same disk.

The SINFONI observations of Class I sources presented in this paper show that ionised and molecular flow components tend to be well collimated. However, on spatial scales of a few hundred AU, H_2 and [Fe II] flow components can possess opening angles of a few tens of degrees (although measurements vary considerably from source to source). Overall, the characteristics of these ionised jets and molecular outflows from Class I protostars seem to mimic those observed in high-resolution observations of HH jets from T Tauri stars. Evolutionary effects, as a source transitions from a deeply embedded protostar to an optically-visible T Tauri star, seem to have little effect on certain jet parameters, such as the opening angle or Mach number.

Acknowledgements. T.P.R. would like to thank Science Foundation Ireland who provided funding for this research under contract 07/RFP/PHYF790. We also acknowledge the anonymous referee for his/her detailed review of this article.

References

Agra-Amboage, V., Dougados, C., & Cabrit, S. 2009, in Protostellar Jets in Context, ed. K. Tsinganos, et al. (Berlin: Spinger-Verlag), 477
Antoniucci, S., Nisini, B., Giannini T., & Lorenzetti, L. 2008, A&A, 479, 503
Arce, H. A., & Sargeant, A. I. 2006, ApJ, 646, 1070
Aspin, C. A., & Sandell, G. 1994, A&A, 288, 803
Aspin, C. A., Reipurth, B., Herczeg, G. J., & Capak, P. 2010, ApJ, 719, L50
Bacciotti, F., & Eislöffel, J. 1999, A&A, 350, 917
Bally, J., Devine, D., & Reipurth, B. 1996, ApJ, 473, L49
Bary, J. S., Matt, S. P., Skrutskie, M. F., et al. 2008, ApJ 687, 376
Beck, T. L. 2007 AJ, 133, 1673
Beck, T. L., McGregor, P. J., Takami, M., & Pyo, T.-S. 2008, ApJ, 676, 472
Beck, T. L., Bary, J. S., & McGregor, P. J. 2010, ApJ, 722, 1360
Benisty M., Malbet, F., Dougados, C., et al. 2010, A&A, 517, L3
Bevington, P. R., & Robinson, K. 1992 in Data Reduction and Error Analysis for the Physical Scientist, 2nd edn. (New York: McGraw-Hill), 198
Biscaya, A. M., Rieke, G. H., Narayanan, G., Luhman, K. L., & Young, E. T. 1997, ApJ, 491, 359
Cabrit, S. 2009 in Protostellar Jets in Context, ed. K. Tsinganos et al. (Berlin: Spinger-Verlag), 247
Cabrit, S., Codella, C., Gueth, F., et al. 2007, A&A, 468, L29
Caratti o Garatti, A., Giannini, T., Nisini, B., & Lorenzetti, D. 2006, A&A, 449, 1077
Caratti o Garatti, A., Froebrich, D., Eislöffel, J., Giannini, T., & Nisini, B. 2008, A&A, 485, 137
Carr, J. S. 1989, ApJ, 345, 522
Chrysostomou, A., Hobson, J., Davis, C. J., Smith, M. D., & Berndsen, A., 2000, MNRAS, 314, 229
Chrysostomou, A., Bacciotti, F., & Nisini, B. 2008, A&A, 482, 57
Chandler, C. J., Carlstrom, J. E., Scoville, N. Z., Dent, W. R. F., & Geballe, T. R. 1990, ApJ, 412, L71
Coffey, D., Bacciotti, F., Podio, L., & Nisini, B. 2010, ApJ, 719, 505
Davis, C. J., Ray, T. P., Eislöffel, J., & Corcoran, D. 1997, A&A, 324, 263
Davis, C. J., Ray, T. P., Desroches, L., & Aspin, C. 2001, MNRAS 326, 524
Davis, C. J., Whelan, E., Ray, T. P., & Chrysostomou, A. 2003, A&A, 397, 693
Davis, C. J., Varricatt, W. P., Todd, S. P., & Ramsay Howat, S. K. 2004, A&A, 425, 981

Davis, C. J., Nisini, B., Takami, M., et al. 2006, ApJ, 639, 969
Davis, C. J., Gell, R., Khanzadyan, T., Smith, M. D., & Jenness, T. 2010, A&A, 511, A24
Doppmann, G. W., Greene, T. P., Covey, K. R., & Lada, C. J. 2005, AJ, 130, 1145
Dougados, C., Cabrit, S., Lavalley, C., & Ménard, F. 2000, A&A, 357, L61
Eislöffel, J., & Mundt, R. 1992, A&A, 263, 292
Eislöffel, J., Guenther, E., Hessman, F. V., et al. 1991, ApJ, 383, L19
Fernández, M., & Comerón, F. 2001, A&A, 380, 264
Ferreira, J. 1997, A&A, 319, 340
Ferreira, J., Dougados, C., & Cabrit, S. 2006, A&A, 453, 785
Garcia, P. J.V., Ferreira, J., Cabrit, S., & Binette, L. 2001, A&A, 377, 589
Garcia Lopez, R., Nisini, B., Giannini, T., et al. 2008, A&A, 487, 1019
Giannini, T., Nisini, B., Caratti o Garatti, A., & Lorenzetti, D. 2002, ApJ, 570, L33
Giannini, T., McCoey, C., Caratti o Garatti, A., et al. 2004, A&A, 419, 999
Giannini, T., Calzoletti, L., Nisini, B., et al. 2008, A&A, 481, 123
Gredel, R. 1992, A&A, 266, 439
Gredel, R. 2006, A&A, 457, 157
Gredel, R. 2007, A&A, 474, 941
Greene, T. P., & Lada C. J. 1996, AJ, 112, 2184
Hamann, F., Simon, M., Carr, J. S., & Prato, L. 1994, ApJ, 436, 292
Hartigan, P., Edwards, S., & Pierson, R. 2004, ApJ, 609, 261
Hirano, N., Ho, P. T. P., Liu, S.-Y., et al. 2010, ApJ, 717, 58
Hirth G., Mundt, R., & Solf, J. 1997, A&AS, 126, 437
Hummer, D. G., & Storey, P. J. 1987, MNRAS, 224, 801
Kraus, S., Hofmann, K.-H., Benisty, M., et al. 2008, A&A, 489, 1157
Koorneef, J. 1983, A&A, 128, 84
Lada, C. J., & Adams, F. C. 1992, ApJ, 393, 278
Lee, C.-F., Mundy, L. G., Reipurth, B., Ostriker, E. C., & Stone, J. M. 2000, ApJ, 542, 925
Lee, C.-F., Ho, P. T. P., Bourke, T. L., et al. 2008, ApJ, 685, 1026
Lee, C.-F., Hasegawa, T. I., Hirano, N., et al. 2010, ApJ, 713, 731
Lorenzetti, D., Giannini, T., Vitali, F., Massi, F., & Nisini, B. 2002, ApJ, 564, 839
Lorenzetti, D., Larionov, V. M., Giannini, T., et al. 2009, ApJ, 693, 1056
Martin, S. C. 1997, ApJ, 478, L33
Martín-Hernández, N. L., Bik, A., Puga, E., Nürnberger, D. E. A., & Bronfman, L. 2008, A&A, 489, 229
Matt, S., & Pudritz, R. 2008a, in 14th Cambridge Workshop on Cool Stars, Stellar Systems and the Sun, ed. G. T. van Belle, ASP Conf. Ser., 384, 339
Matt, S., & Pudritz, R. 2008b, ApJ, 678, 1109
Meyer, M. R., Calvet, N., & Hillenbrand, L. A. 1997, AJ, 109, 1682
Movsessian, T. A., Magakian, T. Y., Moiseev, A. V., & Smith, M. D. A&A, 508, 773
Najita, J., Carr, J. S., & Tokunaga, A. T. 2003, ApJ, 456, 292
Nisini, N., Caratti o Garatti, A., Giannini, T., & Lorenzetti, D. 2002, A&A, 393, 1035
Nisini, N., Antoniucci, S., & Giannini, T. 2004, A&A, 421, 187
Nisini, N., Antoniucci, S., Giannini, T., & Lorenzetti, D. 2005 A&A, 429, 543
Noriega-Crespo, A., Cotera, A., Young, E., & Chen, H. 2002, ApJ, 580, 959
Nussbaumer, H., & Storey, P. J. 1988, A&A, 193, 327
Ouyed, R., & Pudritz, R. E. 1994, ApJ, 423, 754.
Podio L., Bacciotti, F., Nisini, B., et al. 2006, A&A, 456, 189
Pontoppidan, K. M., Blake, G. A., van Dishoeck, E. F., et al. 2008, ApJ, 684, 1323
Pudritz, R. E., & Norman, C. A. 1986, ApJ, 301, 571
Pudritz, R. E., Ouyed, R., Fendt, Ch., & Brandenburg, A. 2007, in Protostars and Planets V, ed. B. Reipurth, D. Jewitt., & K. Keil (Tucson: University of Arizona Press), 277
Pyo, T.-S., Kobayashi, N., Hayashi, M., et al. 2003, ApJ, 590, 340
Pyo, T.-S., Hayashi, M., Kobayashi, N., et al. 2005, ApJ, 618, 817
Pyo, T.-S., Hayashi, M., Kobayashi, N., et al. 2006, ApJ, 649, 836
Pyo, T.-S., Hayashi, M., Kobayashi, N., Terada, H., & Tokunaga, A. T. 2009, ApJ, 694, 654
Ray, T. P. 2000, Ap&SS, 272, 115
Ray, T. P., Mundt, R., Dyson, J. E., Falle, S. A. E. G., & Raga A. C. 1996, ApJ, 468, L103
Reipurth, B. 1989, A&A, 220, 249
Reipurth, B., & Aspin, C. A. 1997, AJ, 114, 2700
Reipurth, B., Yu, K. C., Heathcote, S., Bally, J., & Rodríguez, L. 2000 AJ, 120, 449
Reipurth, B., Heathcote, S., Morse, J., Hartigan, P., & Bally, J. 2002, AJ, 123, 362
Rieke G. H., & Lebofsky, M. J. 1985, ApJ, 288, 618
Safier, P. N. 1993, ApJ, 408, 115
Saucedo, J., Calvet, N., Hartmann, L., & Raymond, J. 2003, ApJ, 591, 275
Schwartz, R. D., Schultz, A. S. B., Cohen, M., & Williams, P. M. 1995, ApJ, 446, 318
Shang, H., Glassgold, A. E., Shu, F. H., & Lizano, S. 2002, ApJ, 564, 853
Shang H., Li, Z.-Y, & Hirano, N. 2007, in Protostars and Planets V, ed. B. Reipurth, D. Jewitt., & K. Keil (Tucson: University of Arizona Press), 261
Shu, F., Ruden, S. P., Lada, C. J., & Lizano, S. 1991, ApJ, 370, L31
Simon, T., Andrews, S. M., Rayner, J. T., & Drake, S. A. 2004, ApJ, 611, 940
Smith, M. D., Davis, C. J., & Lioure, A. 1997, A&A, 327, 1206
Storey, P. J., & Hummer, D. G. 1995, MNRAS, 272, 41
Takami, M., Bailey, J., Gledhill, T. M., Chrysostomou, A., & Hough, J. H. 2001, MNRAS, 323, 177
Takami, M., Chrysostomou, A., Ray, T. P., et al. 2004, A&A, 416, 213
Takami, M. Chrysostomou, A., Ray, T. P., et al. 2006, ApJ, 641, 357
Takami, M., Beck, T. L., Pyo, T.-S., McGregor, P., & Davis, C. J. 2007, ApJ, 670, L33
Tatulli, E., Isella, A., Natta, A., et al. 2007, A&A, 464, 55
Whelan, E., Ray, T. P., & Davis, C. J. 2004, A&A, 417, 247
Whelan, E. T., Ray, T. P., & Bacciotti, F. 2009, ApJ, 691, L106
Whelan, E., T., Dougados, C., Perrin, M. D., et al. 2010, ApJ, 720, L119
Wolniewicz, L., Simbotin, I., & Dalgarno, A. 1998, ApJS, 115, 293
Woitas, J., Ray, T. P., Bacciotti, F., Davis, C. J., & Eislöffel, J. 2002, ApJ, 580, 366
Yun, J. L., Santos, C. A., Clemens, D. P., et al. 2001, A&A, 372, L33

Pages 20 to 23 are available in the electronic edition of the journal at http://www.aanda.org

Appendix A: The effects of differential refraction on source position

In images extracted from each data cube the nominal "source" position was found to shift slightly with wavelength. This shift is largely due to extinction, although differential refraction and/or imperfect cube construction from the 2-dimensional spectral images obtained with the IFS could also contribute.

To investigate this possibility, we examined images extracted from our standard star observations. Six images spread across the H and K-bands were extracted from seven standard star data cubes. We found that the x and y positions of the standard (measured from 2-dimensional Gaussian fits) shifted very slightly with wavelength; a tight linear correlation was identified for each standard star: $\Delta x = S_x \times \delta\lambda$ and $\Delta y = S_y \times \delta\lambda$ (where Δx and Δy are the shift in pixels, λ is the wavelength in microns, and S is the slope of the linear fit). However, S_x and S_y were not the same for all standard stars. Rather, these proved to be a function of airmass, AM, as expected for differential refraction, with $S_x = 3.5{-}2.38 \times AM$ and $S_y = 1.0{-}0.55 \times AM$. Overall, this effect was mild: we found that at low airmass, between [Fe II] and Brγ (increasing wavelength), the source shifted down and to the right by only 0.45 pix, 0.21 pix (0.022″, 0.011″), at intermediate airmass the shift is insignificant in both x and y, while at high airmass the shift is to the left by 0.41 pix, 0.01 pix (0.021″, 0″). These shifts are very small when compared to the offsets measured in Table 2 and essentially only apply to the [Fe II] offsets. They have therefore not been applied to the data.

Appendix B: *H* and *K*-band line flux measurements

Tables B.1 and B.2 list the observed line intensities measured towards each outflow source from the spectra displayed in Figs. 5 and 6.

Appendix C: H_2 excitation diagrams

Molecular hydrogen excitation diagrams may in principal be used to simultaneously estimate the gas excitation temperature and the extinction towards the line-emitting region (e.g. Nisini et al. 2002; Caratti o Garatti et al. 2006).

In thermalised gas at a single temperature, all of the points in the H_2 excitation diagram will lie on a single straight line, the slope of which is a measure of the temperature. In reality, when emission lines from a range of ro-vibrational states are detected, the full diagram is better fit with a curve (Schwartz et al. 1995; Gredel 2006, 2007), or by a separate straight line for each vibrational state (e.g. Giannini et al. 2002; Caratti o Garatti et al. 2006), since lines from higher vibrational states – which have higher critical densities for collisional excitation by hydrogen atoms – may not be fully thermalised. Moreover, the shocks in outflows are rarely planar so the gas in unresolved bow shocks will not be heated to a single temperature; nor will it be maintained at a single temperature as it flows through the shock front and post-shock cooling zone. However, if one plots column densities derived from lines from only the first few vibrational states, a linear fit is usually quite adequate (e.g. Lorenzetti et al. 2002; Giannini et al. 2004; Davis et al. 2004; Gredel 2006; Caratti o Garatti et al. 2008; Martín-Hernández et al. 2008). By minimising the scatter of points about this line, one can then estimate the extinction.

The column density of a given v, J ro-vibrational level, $N_{v,J}$, is related to the line intensity, $I(vJ \rightarrow v'J')$ (measured in W m^{-2}), the wavelength of the transition, λ (in microns), and the $v, J \rightarrow v', J'$ transition probability, $A(vJ \rightarrow v'J')$, by:

$$N_{v,J} = \frac{I(vJ \rightarrow v'J')}{A(vJ \rightarrow v'J')} \left(\frac{4\pi}{hc}\right) \lambda. \quad \text{(C.1)}$$

In thermodynamic equilibrium, the ratio of column densities between two levels, $N_{v,J}$ and $N_{v',J'}$, is given by the Boltzmann equation:

$$\frac{N_{v,J}}{N_{v',J'}} = \frac{g_{v,J}}{g_{v',J'}} e^{-\Delta E/kT_{ex}} \quad \text{(C.2)}$$

where ΔE is the energy difference between the two levels, $g_{v,J}$ is the statistical weight, and T_{ex} is the excitation temperature.

If we adopt an extinction law of the form $A_\lambda/A_v = (\lambda_v/\lambda)^{1.6}$ (Rieke & Lebofsky 1985), then the column density may be corrected for extinction:

$$N_{v,J}(\text{corr}) = N_{v,J}(\text{obs}) \times 10^{0.4A_v(0.55.10^{-6}/\lambda)^{1.6}}. \quad \text{(C.3)}$$

For a given value of A_v, the (negative) reciprocal of the slope of a linear fit to a plot of $\ln(N_{v,J}/g_{v,J})$ against $E_{v,J}$ (the energy of the v, J ro-vibrational level) yields an estimate of T_{ex}. Increasing A_v will increase the value of $N_{v,J}$(corr) and alter the distribution of points around the fit. Minimising this scatter should then yield an estimate of the extinction towards the line-emission region.

In Fig C.1 we present an excitation diagram for HH 26-IRS; similar plots were generated for the other five H_2 line-emitters in our sample. Over a range of extinction values ($A_v = 0{-}100$) we plot corrected column densities (divided by the statistical weights listed in Table C.1) against upper level energies. An ortho-para H_2 ratio of 3 is assumed throughout (note that a ratio that deviates from the statistical value of 3 would offset the ortho-H_2 and para-H_2 data points with respect to each other; an ortho-para ratio of 3 is in any case usually observed in YSO outflows, e.g. Smith et al. 1997). In each plot we fit the data with a single straight line and a second-order polynomial. We measure the extinction values that yield the least scatter about each fit; from the best linear fit we also measure the excitation temperature (see Fig. C.1 for further details).

Our results are listed in Table C.2. In SVS 13 and HH 999-IRS we had insufficient data to measure A_v (although from the two observed lines we could at least estimate T_{ex} assuming $A_v = 0$; note that T_{ex} is relatively insensitive to A_v). Towards the other four sources a range of values were measured. Excluding the Q-branch emission lines, which are suspect due to their location at the edge of the K-band, had little effect on the results. Excluding the higher-energy lines (lines from the $v > 1$ levels and the 1–0 S(7)–S(9) transitions in the H-band) also had only a subtle effect on extinction estimates, although excitation temperatures were consistently lower, as expected.

Table B.1. *H*-band emission lines detected towards each outflow source from the spectra in Figs. 5 and 7. Values are uncorrected for extinction. Errors are given in brackets.

Species	λ μm	HH 34-IRS $F/F_{\mathrm{Br}\gamma}$[a]	HH 300-IRS $F/F_{\mathrm{Br}\gamma}$[a]	SVS 13 $F/F_{\mathrm{Br}\gamma}$[a]	HH 72-IRS $F/F_{\mathrm{Br}\gamma}$[a]	HH 999-IRS $F/F_{\mathrm{Br}\gamma}$[a]	HH 26-IRS $F/F_{\mathrm{Br}\gamma}$[a]
Mg I	1.488	0.019(0.004)	0.004(0.001)	0.061(0.003)	0.038(0.005)	0.007(0.005)	0.027(0.012)
Mg I	1.503[b]	0.062(0.018)	0.010(0.002)	0.076(0.008)	0.051(0.010)	0.032(0.011)	0.065(0.017)
Mg I	1.505[b]	0.146(0.020)	0.004(0.002)	0.14(0.008)	0.095(0.011)	0.016(0.013)	0.034(0.015)
H I	1.527	<0.016	0.006(0.002)	0.027(0.004)	<0.010	<0.008	<0.014
[Fe II]	1.533[c]	0.551(0.007)	0.014(0.002)	0.047(0.004)	0.257(0.008)	0.010(0.002)	<0.014
H I	1.535[c]	...	...	...	...	...	...
H I	1.544	0.032(0.005)	0.007(0.001)	0.027(0.008)	<0.02	0.005(0.001)	<0.02
?	1.547	0.015(0.005)	<0.002	<0.004	<0.02	<0.004	<0.02
H I	1.556	0.047(0.005)	0.008(0.001)	0.033(0.009)	<0.02	0.006(0.003)	<0.02
?	1.564	0.021(0.005)	<0.001	0.02(0.01)	<0.02	<0.004	<0.02
H I	1.571	0.050(0.005)	0.013(0.001)	0.02(0.01)	<0.02	0.005(0.002)	<0.02
Mg I	1.575[b]	<0.11	0.005(0.002)	<0.05	<0.06	0.007(0.002)	<0.06
Mg I	1.577[b]	<0.09	0.003(0.001)	<0.05	<0.06	0.013(0.002)	<0.06
H I	1.589	0.121(0.019)	0.027(0.001)	0.089(0.013)	0.098(0.008)	0.047(0.002)	0.089(0.06)
[Fe II]	1.600	0.495(0.013)	0.013(0.003)	<0.04	0.328(0.025)	0.03(0.01)	<0.06
H I	1.612	0.084(0.014)	0.045(0.003)	0.077(0.008)	<0.01	0.07(0.02)	<0.06
H I	1.641[b]	0.097(0.016)	0.047(0.004)	0.07(0.01)	<0.01	0.10(0.03)	0.08(0.03)
[Fe II]	1.644[b]	2.25(0.02)	0.056(0.004)	0.07(0.01)	1.29(0.02)	0.10(0.03)	0.06(0.02)
[Fe II]	1.664	0.34(0.01)	0.009(0.004)	<0.02	0.23(0.02)	<0.010	<0.02
[Fe II]	1.677	0.66(0.02)	0.038(0.004)	<0.02	0.43(0.02)	<0.012	<0.02
H I	1.681	0.20(0.02)	0.067(0.004)	0.13(0.01)	<0.08	0.063(0.004)	0.065(0.007)
H_2	1.688	0.10(0.02)	<0.02	<0.02	<0.08	<0.012	0.059(0.008)
Mg I	1.711[c]	...	...	...	...	...	...
[Fe II]	1.712[c]	0.241(0.030)	0.008(0.001)	0.098(0.006)	0.21(0.01)	0.023(0.002)	0.063(0.006)
H_2	1.715	<0.01	<0.002	<0.02	<0.02	<0.008	0.020(0.008)
?	1.734	0.041(0.007)	–	0.03(0.01)	0.069(0.008)	0.033(0.009)	0.047(0.020)
H I	1.737	0.139(0.008)	0.075(0.006)	0.16(0.02)	0.063(0.008)	0.096(0.008)	0.085(0.021)
?	1.742	0.081(0.008)	–	0.05(0.02)	0.069(0.007)	<0.02	<0.02
[Fe II]	1.745	0.203(0.007)	0.018(0.007)	<0.02	0.148(0.006)	<0.02	<0.02
H_2	1.748	0.079(0.007)	<0.01	<0.02	0.071(0.006)	<0.02	0.095(0.012)
[Fe II]	1.798	0.34(0.03)	<0.01	<0.04	0.28(0.04)	<0.02	<0.04
[Fe II]	1.801	0.42(0.03)	<0.01	<0.04	0.42(0.04)	<0.02	<0.04
[Fe II]	1.810	1.08(0.04)	0.043(0.011)	<0.04	0.65(0.04)	<0.02	<0.04
H I	1.818	0.65(0.04)	0.26(0.03)	0.58(0.04)	0.70(0.20)	0.61(0.04)	<0.04

Notes. [(a)] Line flux relative to Brγ, which we measure at $4.02(\pm0.05) \times 10^{-17}$ W m^{-2} in HH 34-IRS, $13.5(\pm0.20) \times 10^{-17}$ W m^{-2} in HH 300-IRS, $249(\pm5.0)\times10^{-17}$ W m^{-2} in SVS 13, $24.4(\pm0.2)\times10^{-17}$ W m^{-2} in HH 72-IRS, $102(\pm2.5)\times10^{-17}$ W m^{-2} in HH 999-IRS, $7.47(\pm0.27)\times10^{-17}$ W m^{-2} in HH 26-IRS and $50.1(\pm4.6) \times 10^{-17}$ W m^{-2} in HH 83-IRS. [(b)] Lines blended – flux measured from a 2-component Gaussian fit. [(c)] Two lines unresolved; in some sources [Fe II] flux possibly contaminated by H I at 1.535 μm and/or Mg I at 1.711 μm.

Table B.2. *K*-band emission lines detected towards each outflow source from the spectra in Figs. 6 and 7. Values are uncorrected for extinction. Errors are given in brackets.

Species	λ μm	HH 34-IRS $F/F_{Br\gamma}$ [a]	HH 300-IRS $F/F_{Br\gamma}$ [a]	SVS 13 $F/F_{Br\gamma}$ [a]	HH 72-IRS $F/F_{Br\gamma}$ [a]	HH 999-IRS $F/F_{Br\gamma}$ [a]	HH 26-IRS $F/F_{Br\gamma}$ [a]
H I	1.945	0.77(0.06)	0.59(0.03)	0.84(0.04)	...	0.67(0.04)	1.07(0.08)
He I	1.951[b]	0.13(0.06)	<0.04	...	...	...	...
He I	1.954[b]	0.10(0.05)	<0.04	...	...	...	...
H_2	1.958	0.64(0.05)	0.11(0.02)	0.05(0.02)	0.58(0.08)	0.16(0.04)	0.55(0.05)
[Fe II]	1.968	0.09(0.02)	<0.02	<0.03	0.44(0.10)	<0.04	...
Ca I	1.978	0.19(0.02)	0.06(0.01)	0.20(0.02)	0.38(0.07)	0.07(0.02)	0.15(0.03)
Ca I	1.987	0.12(0.02)	<0.03	0.13(0.02)	0.62(0.09)	0.09(0.02)	0.24(0.04)
H_2	2.004	<0.04	<0.02	<0.1	0.20(0.08)	...	<0.08
[Fe II] ?	2.007	0.30(0.02)	<0.02	<0.1	0.45(0.05)	...	<0.08
[Fe II]	2.016	0.27(0.02)	0.019(0.008)	<0.05	0.32(0.06)	...	<0.08
H_2	2.034	0.12(0.02)	0.04(0.01)	<0.05	0.50(0.08)	<0.04	0.29(0.03)
[Fe II]	2.047	0.33(0.02)	0.041(0.007)	<0.05	0.65(0.06)	<0.04	<0.08
H_2	2.074	<0.05	<0.01	<0.04	<0.1	<0.04	0.24(0.04)
Mg I ?	2.108	<0.05	<0.01	0.07(0.02)	<0.1	<0.04	<0.06
Mg I ?	2.110	<0.05	<0.01	0.04(0.015)	<0.1	<0.04	<0.06
Al I ?	2.118	<0.05	<0.01	0.08(0.014)	0.21(0.07)	<0.05	0.10(0.04)
H_2	2.122	0.51(0.01)	0.666(0.007)	0.14(0.01)	1.04(0.07)	0.12(0.02)	1.04(0.03)
[Fe II]	2.133	0.19(0.01)	0.012(0.005)	<0.03	0.20(0.06)	<0.04	<0.05
H_2	2.154	<0.02	<0.01	<0.03	<0.15	<0.04	<0.05
H I	2.166	1.0(0.01)	1.0(0.01)	1.0(0.02)	1.0(0.01)	1.0(0.01)	1.0(0.01)
Ti I?	2.179	<0.03	<0.015	<0.05	0.34(0.08)	<0.05	0.16(0.03)
H_2	2.201	<0.03	<0.015	<0.04	...	<0.05	0.05(0.02)
Na I	2.207[b]	0.16(0.02)	0.061(0.008)	0.27(0.03)	0.64(0.10)	0.20(0.03)	0.29(0.03)
Na I	2.209[b]	0.14(0.02)	0.090(0.009)	0.22(0.03)	0.44(0.10)	0.22(0.03)	0.25(0.03)
H_2	2.224	0.507(0.02)	0.10(0.02)	<0.1	0.60(0.09)	<0.08	0.38(0.07)
[Fe II]	2.244	0.109(0.014)	<0.02	<0.1	0.35(0.09)	<0.08	<0.15
H_2	2.248	0.036(0.014)	<0.04	<0.1	<0.2	<0.08	<0.15
[Fe II]	2.254	0.127(0.01)	<0.04	<0.1	<0.2	<0.08	<0.15
Ca I ?	2.263	0.02(0.01)	...	<0.1	<0.2	<0.08	<0.15
Ca I ?	2.267	0.02(0.01)	...	<0.1	<0.2	<0.08	<0.15
CO 2-0	2.294	3.33(0.6)	1.55(0.7)	4.5(1.0)	13.0(3.0)	8.4(0.9)	10.2(1.5)
CO 3-1	2.323	3.63(0.6)	1.64(0.7)	5.2(1.2)	15.4(3.0)	10.6(1.0)	11.2(2.0)
CO 4-2	2.354	3.34(0.8)	1.61(1.2)	4.9(1.5)	17.3(5.0)	11.5(1.5)	12.5(2.0)
CO 5-3	2.383	2.82(1.0)	...	5.8(2.0)	15.4(6.0)	11.1(3.0)	12.4(3.0)
H_2	2.407	0.73(0.11)	0.10(0.04)	<0.3	1.64(0.05)	<0.2	1.25(0.24)
H_2	2.424	0.72(0.09)	0.16(0.06)	<0.5	...	...	1.58(0.24)

Notes. [a] Line flux relative to Brγ, see Table B.1 for details. [b] Lines blended – flux measured from a 2-component Gaussian fit.

Table C.1. H_2 parameters used to generate the excitation diagrams for each outflow source (see e.g. Fig. C.1). Note that not all lines were observed in each source (see Tables B.1 and B.2 for details).

Line	λ (μm)	Statistical[a] Weight, $g_{v,J}$	Transition Probability[b] $A(vJ \rightarrow v'J')$ (s^{-1})
1–0 S(0)	2.223	5	2.53×10^{-7}
1–0 S(1)	2.122	21	3.47×10^{-7}
1–0 S(2)	2.034	9	3.98×10^{-7}
1–0 S(3)	1.958	33	4.21×10^{-7}
1–0 S(7)	1.748	57	2.98×10^{-7}
1–0 S(8)	1.715	21	2.34×10^{-7}
1–0 S(9)	1.688	69	1.68×10^{-7}
2–1 S(1)	2.248	21	4.98×10^{-7}
2–1 S(2)	2.154	9	5.60×10^{-7}
2–1 S(3)	2.073	33	5.77×10^{-7}
2–1 S(4)	2.004	13	5.57×10^{-7}
3–2 S(3)	2.201	33	5.65×10^{-7}
1–0 Q(1)	2.407	9	4.29×10^{-7}
1–0 Q(3)	2.424	21	2.78×10^{-7}

Notes. [a] The statistical weight includes rotational ($g_j = 2J + 1$) and spin ($g_s = 1$ for even-J; $g_s = 1$ for odd-J) degeneracies. [b] From Wolniewicz et al. (1998).

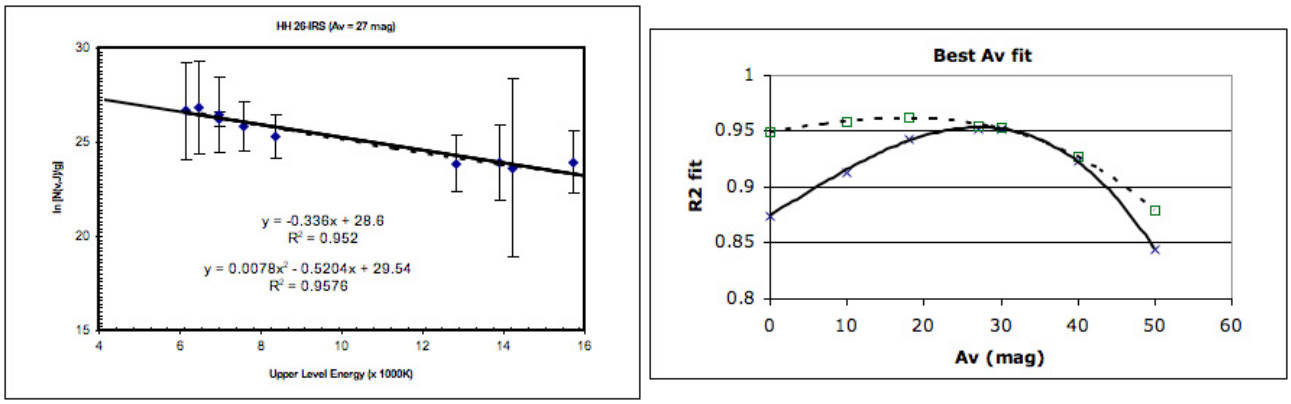

Fig. C.1. The *left-hand panel* shows an H_2 excitation diagram for HH 26-IRS. The data, corrected for extinction (A_v = 27 in this case), have been fitted with a straight line and a second-order polynomial (dashed line). The equations describing each fit are displayed; the R^2 values represent the square of the correlation coefficient associated with each fit. Plots over a range of A_v values were generated and R^2 measured for the two fits in each case. The *right-hand panel* shows a plot of R^2 against A_v. Data from the linear and polynomial fits are represented by a cross and an open square, respectively; the full and dashed lines represent third-order polynomial fits to these data. The peak in each curve in the right-hand plot marks the extinction associated with the greatest value of R^2, which in turn is associated with the least scatter about the linear and polynomial fits in the excitation diagram.

Table C.2. Extinction and H_2 excitation temperature derived for each source from the line detections listed in Tables B.1 and B.2.

Source	A_v(poly)[a] (mag)	A_v(line)[a] (mag)	T_{ex}[a] (K)	A_v(poly,noQ)[b] (mag)	A_v(line,noQ)[b] (mag)	T_{ex}(noQ)[b] (K)	A_v(line,v = 1)[c] (mag)	T_{ex}(v = 1)[c] (K)
HH 34-IRS	6	0	1616	0	0	1667	0	975
HH 300-IRS	27	10	5565	24	6	4629	0	1031
SVS 13	...	...	8028[d]	...	...	...	...	...
HH 72-IRS	0	0	1355	0	0	1396	0	868
HH 999-IRS	...	...	3218[d]	...	...	...	...	...
HH 26-IRS	18	27	2976	17	27	3077	24	1339

Notes. [(a)] Extinction values derived by minimising the scatter of data points about a second-order polynomial fit and a linear fit, respectively; the excitation temperature is measured from the slope of the linear fit. [(b)] A_v and T_{ex} derived from second-order polynomial and linear fits to all lines *excluding* the Q-branch transitions. [(c)] A_v and T_{ex} derived from linear fits to only transitions from the v = 1 state. [(d)] Value based on only two line intensities.